ENERGY MATERIALS RESEARCH

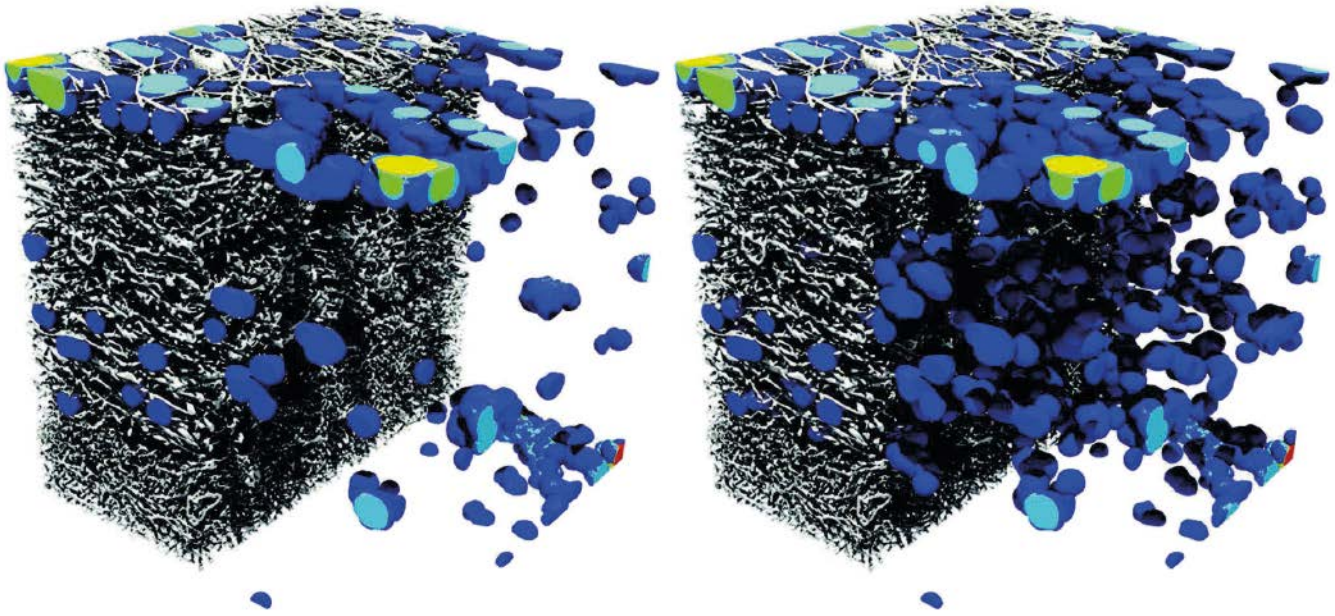

WILEY

Imprint

Boschstr. 12, 69469 Weinheim,
Germany
Email: info@wiley-vch.de

Carl Zeiss Microscopy GmbH
Carl-Zeiss-Promenade 10,
07745 Jena,
Germany
www.zeiss.com/microscopy

Editor-in-Chief:
Dr. Birgit Washburn

Editor:
Dr. Martin Friedrich

Ad Sales:
Dr. Stefanie Krauth

Editorial

How does energy touch our lives? From the food we eat to the way we power our homes, consume information or move around, energy plays a vital role in nearly every aspect of our lives. Energy lights our schools and homes, connects us with friends and loved ones, and is the fuel that drives our societies today. Indeed, it is so common that we often take its presence for granted. But the more we become aware of the consequences of energy production, the more we look at the source of this energy.

There is a good chance that you are reading this compendium on an electronic device powered by a battery. But have you thought about where this energy comes from? Or the scientific breakthroughs needed to bring this technology into your hands? Teams and generations of scientists have been working to improve the way energy is generated, stored, converted, and used today. Recently, the importance of this work was recognized when the Royal Swedish Academy of Sciences awarded the Nobel Prize in Chemistry to Goodenough, Whittingham, and Yoshino for the development of lithium ion batteries.

This booklet aims to give you an overview of recent achievements in energy materials research. A brief introduction details some advanced microscopy techniques from ZEISS and their specific benefits for your research. This is followed by a selection of peer-reviewed articles from various WILEY journals, condensed into a digestible format with links to the original article DOIs.

In a concluding interview, Professor Paul Shearing from University College London shares his views on current challenges and future developments in microscopy applications for energy materials.

Dr. Benjamin Tordoff
Head of Materials Science Sector,
ZEISS Research Microscopy Solutions

Contents

Introduction

Developing Energy Devices for Mobility and Sustainability

As **natural resources** become increasingly scarce and the demand grows for more portable, reliable, safe and sustainable forms of energy, scientists face new **challenges in materials research and engineering**. Devices ranging from solar cells to batteries, fuel cells and next generation nuclear reactors—and the often highly heterogeneous materials they contain—present a paradigm shift in shaping the way energy is generated, stored, and converted. Today's researchers focus on extending the lifetime, improving the efficiency, and ensuring safe operation of these devices. As the properties and performance of these materials and devices is intrinsically linked to their micro- and nano-structure, microscopy plays a critical role, complementing techniques such as thermal, mechanical, or electrochemical analysis. Beyond traditional 2D or 3D structural inspection, multi-scale, multi-modal imaging and analysis approaches lead to a comprehensive understanding of the links between structure, chemistry and performance. This deep understanding paves the way towards designing novel materials and devices, and lights the way to a bright energy future for our planet.

Characterization is More Than Just Imaging

In lithium ion batteries (LIB), for example, relevant device and material features spanning across many orders of magnitude in length affect the ultimate performance of the battery. Measuring the **geometric architecture** of the LIB, inspecting the package of intact LIBs, **quantifying particles**, **voids**, and porosity, and mapping the **chemical composition and reactivity** on a micro- or even a nanometer scale are of keen interest. (Fig. 1)

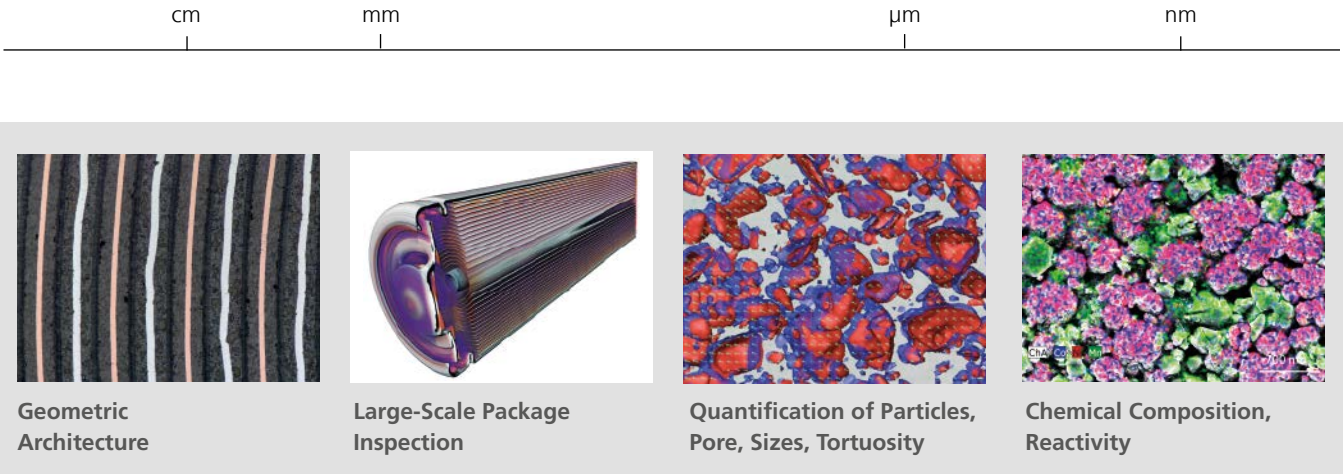

Figure 1: *Relevant features of batteries or their components spanning length scales from centimeters to nanometers characterized by multiple imaging and analytical techniques. From left to right, optical micrograph of a polished battery cross section, X-ray microscopy image of an intact battery cell, X-ray microscopy image of battery cathode particles, and scanning electron microscopy image overlaid with energy dispersive spectroscopy image of mixed chemistry battery cathode particles.*

Large scale architectures and general microstructural information can be obtained quickly and at high resolution using stereo, digital, or widefield light microscopy. Kerr microscopy allows for visualization of magnetic domains in materials for new electric vehicle motors, while confocal laser scanning microscopes enable failure analysis and surface profiling, if needed. For even higher magnifications, e.g. to characterize micro- and nanometer scaled defects in battery electrode materials, or when imaging sensitive material like graphite or polymers, an SEM with outstanding low voltage performance provides reliable and robust information. (Fig. 2 and Fig. 3)

Materials researchers profit from non-destructive **inspection** of the whole, intact battery when performing large-scale inspection in 3D or even 4D – covering also time lapse experiments – using high resolution X-ray microscopy (XRM). XRM enables the characterization of a 3D volume in micro- or nanoscale easily and non-destructively, allowing studies to track microstructural changes over many cycles. (Fig. 4)

Particle and void sizes or tortuosity inside of the battery can also be **quantified** with an XRM. The tortuosity, a value that describes diffusion and fluid flow in porous media, is calculated using geometric input from a high resolution 3D X-ray image. Going from micro- to nanometer scaled structures, researchers combine more than one technique. One example is combining XRM with FIB-SEM in correlative workflows to investigate e.g. inclusion microstructure and chemistry in battery cathodes. The experiment is started by scanning a larger volume with X-ray microscopy non-destructively, followed by navigating to the identified region of interest using connected solutions for correlative microscopy. Finally, in-depth FIB-SEM analysis at high resolution reveals fine microstructural features. (Fig. 5 and Fig. 6)

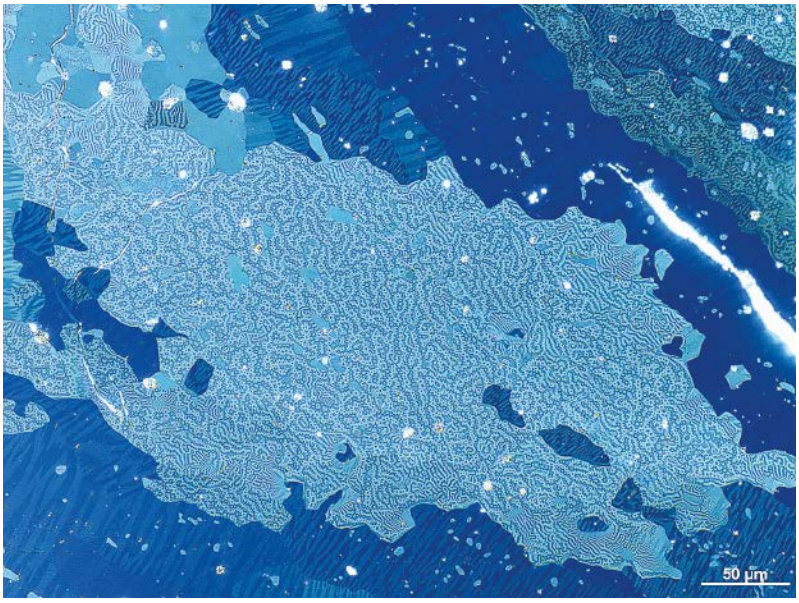

Figure 2: *Kerr microscopy micrograph of a permanent magnet used in new electric vehicle motors. Colors indicate magnetic domain orientations.*

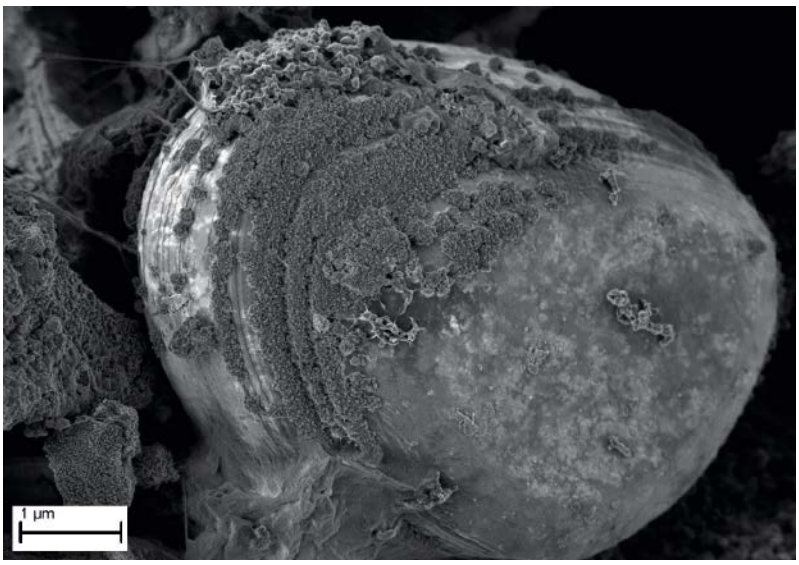

Figure 3: *Scanning electron micrograph of a $LiCoO_2$ battery cathode particle showing surface morphology, polymer binder, and conductive additives. Image collected at extremely low voltage (600 V) with an Inlens secondary electron detector.*

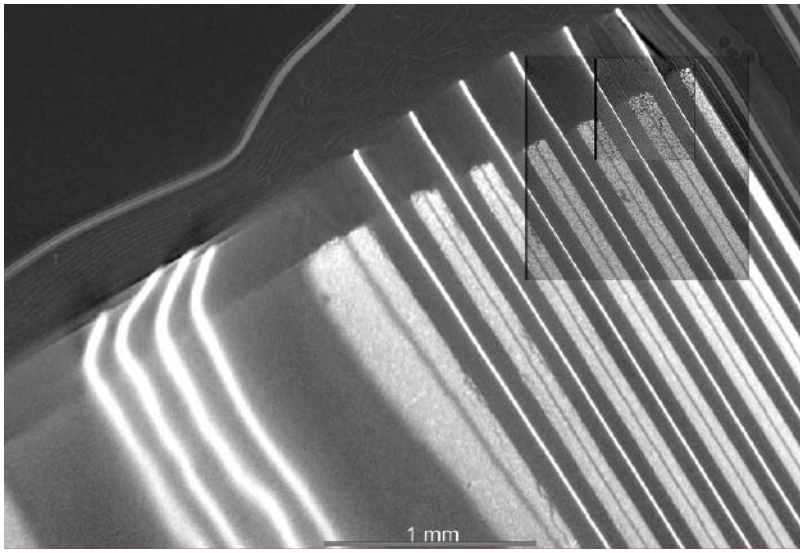

Figure 4: *Three X-ray microscopy micrographs (compare overview and two inlays) at progressively higher resolution showing internal features in an intact commercial pouch cell battery.*

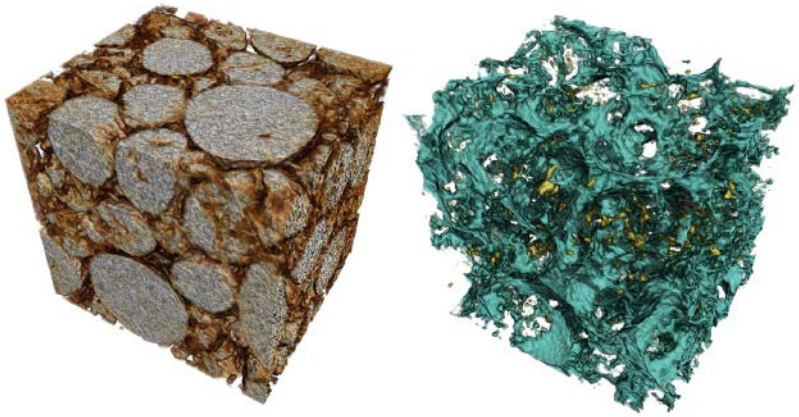

Figure 5: *Nanometer-scaled 3D X-ray microscopy images showing cathode particles from a commercial lithium ion battery (left) along with the corresponding pore network surrounding the particles (right).*

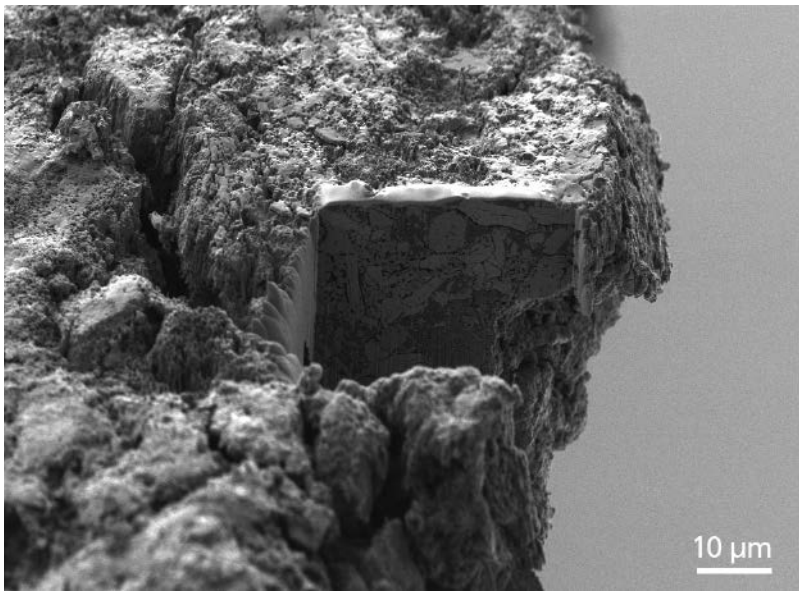

Figure 6: *Scanning electron micrograph of a $LiMn_2O_4$ lithium ion battery cathode after cutting and polishing with a focused ion beam scanning electron microscope revealing a cross-section through the material to investigate subsurface defects.*

Beyond traditional imaging, **analytic techniques** in SEM, ion microscopy like FIB-SEM or HIM (helium-neon ion microscope) or XRM allow not only for investigations into microstructural features, but the chemical composition of a material. Energy dispersive spectroscopy (EDS), Raman spectroscopy, and secondary ion mass spectroscopy (SIMS) allow for high resolution mapping of chemical and elemental constituents while electron backscatter diffraction (EBSD) maps crystallographic grain orientations. These techniques find applications in energy materials like polymer battery separators, lithium ion battery electrode materials, high temperature metal alloys, and composite materials like fuel cell electrodes and thin film solar cells.

As most energy materials operate in a dynamic, non-ambient environment, measurements under operating conditions are essential. *In situ* stages are available for many of these experimental techniques as well, e.g. for heating or tensile experiments.

As material and device performance depend critically on microstructural properties at multiple length scales, **multi-modal, multi-scale correlative workflows** are opening up windows to a deeper understanding of the structure-property relationship at the core of materials science research. Guided by linked, integrated solutions that include large area imaging, correlative microscopy, post-processing (like machine learning guided segmentation) and seamless transitions between e.g., LM, SEM, Raman and EDS, researchers are leveraging these workflows to make tranformational discoveries in energy materials research.

As we move into the new decade, inclusive research tools that incorporate microstructural, chemical, electrical, and mechanical analytics will enable researchers to push the boundaries of energy materials research and development as they aim to provide a secure energy future. We look forward to seeing what's next and helping to enable tomorrow's breakthroughs! (Fig. 7 and Fig. 8, Fig. 9)

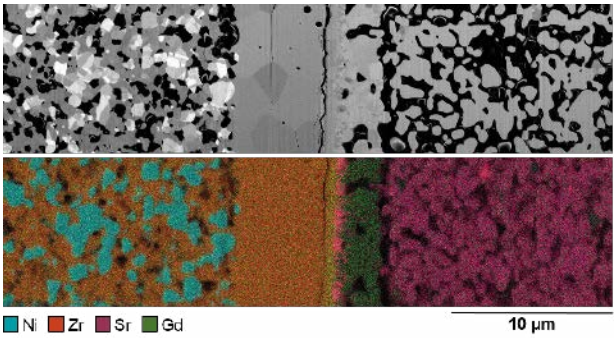

Figure 7: *Scanning electron micrograph from a solid oxide electrolysis cell (top) and elemental distribution in the image from energy dispersive spectroscopy (bottom).*

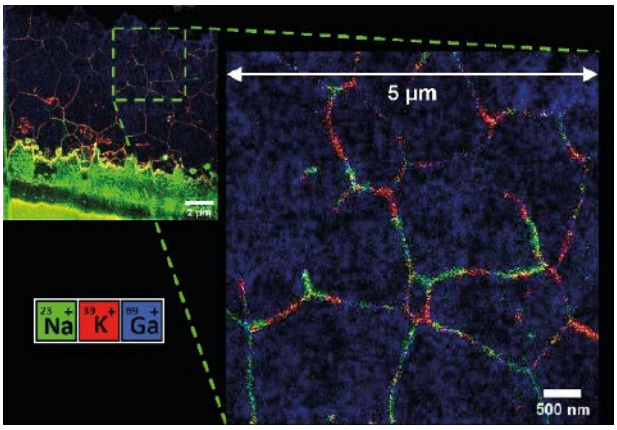

Figure 8: *Composite image of Na, K, and Ga SIMS maps on a CIGS (copper indium gallium selenide) photovoltaic solar cell acquired with a SIMS detector added to ZEISS ORION NanoFab, a helium-neon ion microscope. An area of 5 µm x 5 µm has been zoomed in for more detail, showing elemental distribution along the grain boundaries.*

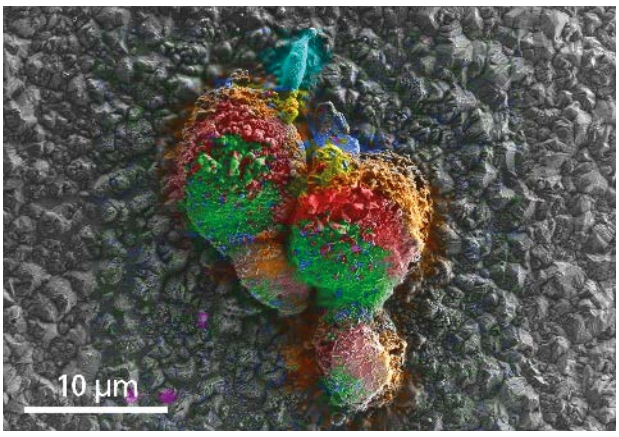

Figure 9: *Electrochemically deposited Li(NiMnCo)O_2 battery particles. Overlay of SEM image and Raman mapping. The overlay of Raman mappings and SEM images enable to combine the findings of structural and chemical properties. Smooth surfaces containing $LiNiMnO_2$: green, rough areas containing $LiMnCoO_2$: orange, and $LiNiMnCoO_2$: red.*

Insights into the Effect of Structural Heterogeneity in Carbonized Electrospun Fibrous Mats for Flow Battery Electrodes by X-Ray Tomography

Kok M. D. R., Jervis R., Brett D. et al.

Electrospun custom made flow battery electrodes were imaged in 3D using X-ray computed tomography (CT). A variety of computational methods and simulations were applied to the images to determine properties including the porosity, fiber size, and pore size distributions as well as the material permeability and flow distributions. The simulations were performed on materials before and after carbonization to determine the effect it has in the internal microstructure and material properties. It was found that the deposited fiber size is constantly changing throughout the electrospinning process. The results also showed that the surfaces of the fibrous material are the most severely altered during carbonization and that the rest of the material remained intact. Pressure driven flow was modeled using the lattice Boltzmann method and excellent agreement with experimental results was found. The simulations coupled with the material analysis also demonstrated the highly heterogeneous nature of the flow. Most of the flow was concentrated to regions with high porosity while regions with low porosity shield other pores and starve them of flow. The importance of imaging these materials in 3D has been revealed.

Electrospinning

Porous media, and specifically fibrous media, are essential to a wide variety of technologies ranging from traditional filtration membranes, to biomedical applications and advanced electrochemical systems. Electrospinning, a method of preparing fibrous media by which nano- and microfibers are "spun" from a solution using a large voltage potential (>10 kV), has become a common means of producing fibrous materials with customized structures. The main appeal of electrospinning, aside from the simplicity of the equipment required, is the tunability of the method, allowing the generation of fibers from as small as tens of nanometers to several micrometers with a wide array of morphologies. In electrochemistry, electrospun materials are being employed in a range of devices, such as lithium-ion battery separators. These mats can also be carbonized to produce electrically conductive materials for use as Li-ion battery anodes, and gas diffusion layers in polymer electrolyte membrane fuel cells. Carbonized electrospun mats were already used as flow-through electrodes in flow batteries. Flow batteries offer a potential solution to grid-scale energy storage due to their reliability, relatively cheap and simple components, and the decoupling of power (determined by the size of the cell) and energy (determined by the volume of electrolyte storage), which makes them flexible to the needs of many different systems.

Tomography

Imaging of the electrospun materials was conducted using a Zeiss Xradia Versa 520 X-ray microscope, operating with a source voltage of either 30 or 40 kV. It was found that a low source voltage and a sample diameter of 1 mm or less was required to obtain a good quality image due to the highly porous and low-Z nature of the materials. 1601–2201 projections of 30 s exposure each were recorded through an angular sample rotation of 360°. Reconstruction of the X-ray transmission images was conducted using a filtered back-projection reconstruction algorithm (XM Reconstructor, Zeiss). Use of a 20x objective lens and binning of 1 yielded a voxel size of 0.36–0.40 µm in the reconstructed 3D data. The grayscale reconstructed volume was then segmented into a binary image using Avizo Fire software (Thermo Fisher Scientific) to designate pixels as either "fiber" or "pore" materials by thresholding based on their grayscale value. These binarized data sets were then exported as image stacks and used as the structures for the computer modeling (Figure 1).

Porosity, fiber size and pore size distributions

This study explored the use of computational methods on 3D tomographic images of electrospun materials, with a specific aim of characterizing the consistency of produced structures. This was the first time that electrospun fibers have been imaged in 3D at this resolution (between 360 and 400 nm per voxel) using this technique. The materials imaged represent 12 and 13 wt% PAN in dimethylformamide (DMF), both "as spun" and after carbonization to make electronically conductive materials for electrochemical applications. Custom image analysis tools allowed for the determination of the fiber size and porosity distributions though the materials, as well as simulated mercury

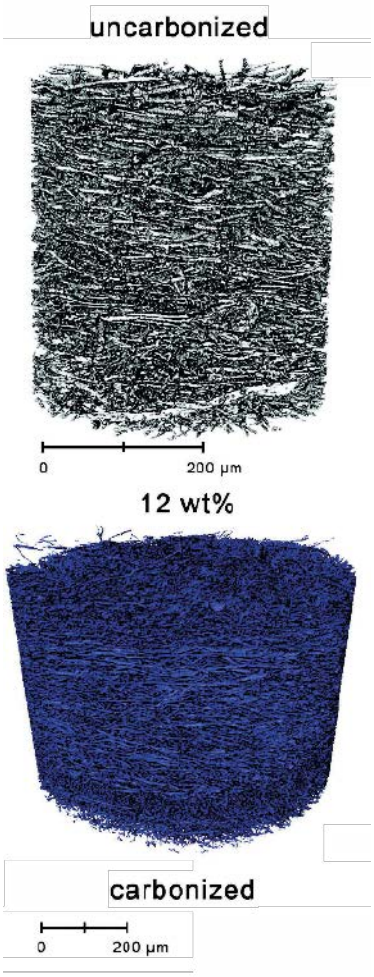

Fig. 1: 3D representations of uncarbonized (top, white) and carbonized (bottom, colored) electrospun materials made from a spin dope containing 12 wt% of Polyacrylonitrile (PAN). The images shown here are rendered from pixels assigned to the "fiber" phase using the threshold segmentation tool in the Avizo software suite, and represent the binarized data sets used in the modeling.

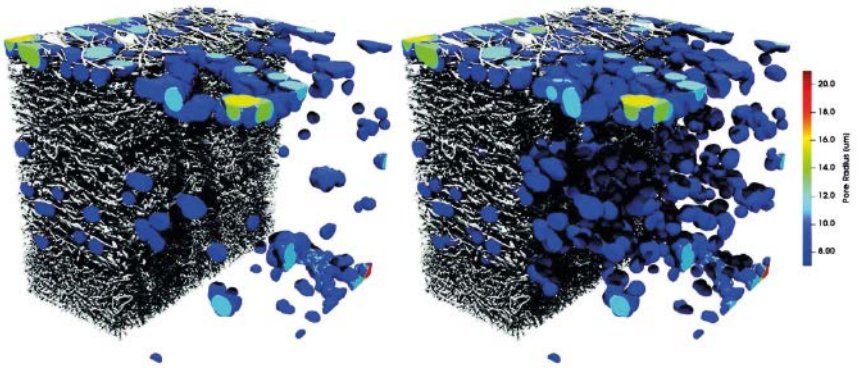

Fig. 2: 3D rendering 12 wt% carbonized material. The image on the left shows the local pore sizes determined by a mercury intrusion porosimeter (MIP) simulation while the right shows the local pore sizes determined by the local thickness method. The pore sizes have been thresholded to the same value in each image to relieve clutter.

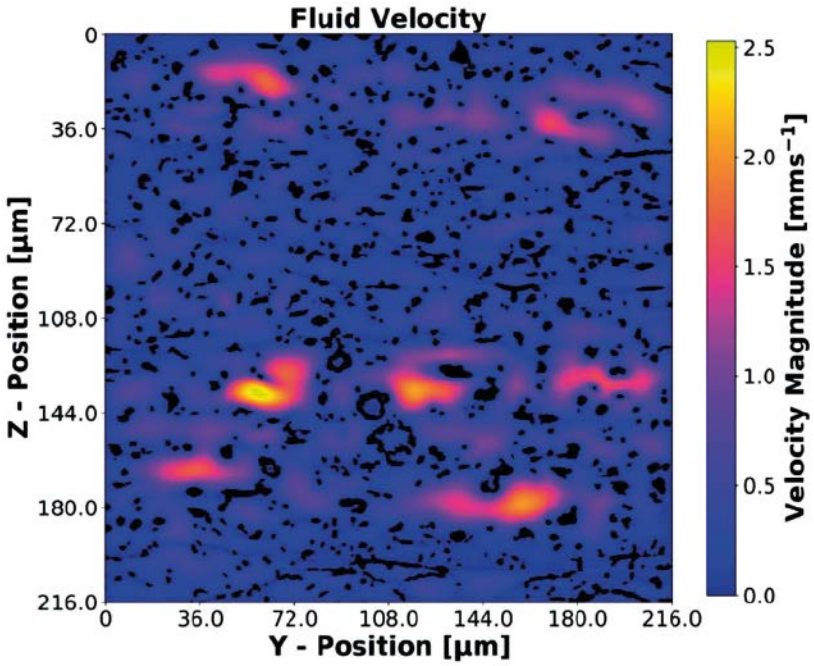

Fig. 3: Fluid velocity through a YZ "slice" of porous material. The fluid is flowing perpendicular to the plane of the image. Zero flow (black) represents the fiber phase. The material shown here is of the 12 wt% carbonized material.

intrusion porosimetry (MIP) experiments and generated pore size distributions. It was found that for both the fiber diameter and the material porosity the only significant variation was in the Z-dimension. Because this dimension corresponded to the electrospinning time, it provided direct evaluation of inconsistent or drifting production conditions. The other two dimensions revealed a very even distribution, which demonstrated the effectiveness of the rotating drum and the rastering of the electrospinning needle to ensure uniform properties.

An example 3D rendering of the 12 wt% carbonized material can be seen in Figure 2. The left of the image shows the local size determined by an MIP simulation while the right shows the local pore sizes determined by the local thickness method. The pore sizes have been thresholded to the same value for each image to relieve clutter. This allowed for the direct comparison of the two images. Anything on the right that does not appear on the left is being affected by shielding and bottlenecking.

The SEM limitation – the advantage of X-ray CT

The fiber diameter distributions showed two interesting characteristics that are both relevant to the common practice of determining material properties from scanning electron microscopy (SEM) images. First, because electrospinning is a dynamic process, the fiber size at either surface can give a very poor representation of the fiber size throughout. It was shown that the size of the fibers can possibly change during the entirety of the spinning process. Which side is imaged under SEM can lead to very different ideas about material properties. More generally, SEM is limited to 2D images but most properties of interest are linked to percolation and therefore require 3D imaging.

The 12 wt% material showed a very even distribution in fiber size before carbonization, but after carbonization the fiber size on the surfaces was significantly lower. The likely cause for this is compression or temperature gradients during the carbonization process, which lead to higher conversion at the edges. This represents a significant issue because had this sample been analyzed with SEM the fiber size, and therefore many material properties, would be incorrect and many assumptions about the carbonization process would be misleading.

Permeability and flow distributions

The flow distribution in the materials was determined using the lattice Boltzmann method. This allowed for the determination of the material permeability, which was compared to experimentally obtained results on the same materials imaged. The LBM permeability showed excellent agreement with the experimental results, which validated the flow distributions. Further analysis was done on the distribution of permeability within the materials and it was shown quite clearly that the largest determining factor for permeability was the material porosity. The permeability and flow distributions obtained demonstrate the effect that heterogeneity can have on the performance of these engineered materials. Small variations in fiber diameter and local porosity can double the material permeability, and these changes can happen on a scale of 10's of micrometers. Imaging these materials with high-resolution X-ray CT provided insights into actual flow that were not available through SEM or continuum modeling alone.

To get a more quantitative picture of the flow heterogeneity, the distribution of flow velocity was analyzed on a voxel-by- voxel basis, as shown in Figure 3 which is a YZ slice of the 3D velocity field. Clearly visible are pockets of high velocity surrounded by regions of low or almost no flow. If this material were used as a flow-through electrode, a significant portion of the reactive surface area would be starved for reactants.

There was a correlation between the distance transform and the velocity; all regions of high flow were traversed by large pores; however, the opposite was not the case. There were large pores in the whole material, which had a very low or even stagnating flow. There were two main causes: The first, known as channeling, was where the regions had starved of flow because the entire flow had concentrated on one area because large pores formed a continuous flow domain. This can be seen very clearly in the lower half of Figure 3, where there are five dominant "pipes" in which most of the flow is concentrated. The second factor closely related to the first was shielding where smaller pores prevented flow from reaching the larger pores.

Summary

Electro-spun electronically conductive fibers were imaged by X-ray CT in 3D with a resolution between 360 and 400 nm per voxel for the first time. It was observed that the only significant deviation in the Z dimension was for both the fiber diameter and the material porosity. It was also shown that the size of the fibres could possibly change during the entire spinning process. The 12 wt% material revealed a very uniform distribution of fiber size prior to carbonization, but after carbonization the fiber size on the surfaces was significantly smaller. It was clearly stated that the largest decisive factor for permeability is material porosity. Small variations in fiber diameter and local porosity could double material permeability, and these changes could occur on a scale of 10's microns. This study demonstrated that only with 3D methods such as X-ray CT can it be achieved to fully decipher the property distribution in the modeling of porous media.

Digest of
Kok M. D. R., Jervis R., Brett D., Shearing P. R., Gostick J. T.; Insights into the Effect of Structural Heterogeneity in Carbonized Electrospun Fibrous Mats for Flow Battery Electrodes by X-Ray Tomography; Small, 2018, 14, 1703616; https://doi.org/10.1002/smll.201703616.

Optimized Design Principles for Silicon-Coated Nanostructured Electrode Materials and their Application in High-Capacity Lithium-Ion Batteries

Auer A., Jonasson N. S. W., Apaydin D. H. et al.

Silicon is considered as one of the most promising electrode materials for next-generation, high-energy-density Li-ion batteries as it demonstrates an exceptionally high specific capacity an order of magnitude beyond that of conventional graphite. The poor capacity retention, caused by the mechanical fracturing of Si because of the extreme volumetric and structural changes upon Li insertion/extraction, has triggered significant attention in the development of Si-coated nano-structures that can accommodate the lithiation-induced strain. In parallel, various spectroscopic studies and simulations have been conducted to understand the details of volumetric expansion, fracture, mechanical stress evolution, and structural changes in Si-coated nanostructures. This publication reported a systematic lithiation/delithiation study of Si-coated, anodically grown, self-organized titanium dioxide (TiO_2) nanotubes (NTs) with different Si-layer thicknesses. It could be demonstrated for the first time that a "sweet spot" for the Si-coating thickness was formed at which the specific lithiation capacity of the composite material reached its maximum, which declined quickly for higher coating thicknesses. Furthermore, the results suggested that such a Si-thickness-dependent optimum in the specific lithiation capacity was immanent to any Si-coated nanostructured electrode.

Challenges for Li-ion batteries

In particular, Si has attracted considerable attention as a promising anode material for Li-ion batteries because of its exceptional theoretical high specific capacity of 3580 mAh g^{-1} for the $Li_{15}Si_4$ phase at room temperature. Despite these preeminent properties, bulk Si anodes face significant challenges because of the large volume changes that occur upon lithiation, which lead to the mechanical fracturing of the active material, accumulation of solid-electrolyte interphase (SEI) layers, and rapid capacity fading during electrochemical cycling. Recently, nanotechnology has been used to achieve a breakthrough to overcome the abovementioned challenges of Si to serve as an anode electrode for Li-ion batteries. Different designs of Si nanomaterials and engineered Si-covered nanostructures, such as nanowires, nanotubes, hollow spheres, and porous nanostructures, which are more resistant to structural degradation by virtue of their small nanoscale sizes, have demonstrated the stable cycling performance of Si. Among many other nanostructures, TiO_2 NTs, which promise to provide important advantages in terms of cost effectiveness, safety, and environmental compatibility, have been applied successfully.

The anodically grown, self-organized TiO_2 NTs are supported on Ti and were annealed under reducing conditions to carbon containing anatase TiO_{2-x}-C NTs. The TiO_{2-x}-C NTs provide 1D electron transport towards the Ti metal substrate, which serves directly as the current collector. Therefore, the utilization of anatase TiO_{2-x}-C NTs eliminates the need to use conductive carbon to increase the electronic conductivity, which would, consequently, decrease the gravimetric capacity of the electrode. Although Si is known to demonstrate the highest theoretical specific capacity for Li intercalation, the TiO_2 NTs support has substantial Li insertion capabilities. The Li insertion potential of TiO_2 is 1.2–2.0 V versus Li. Although it has been shown that TiO_2 is prone to surface film formation in most electrolytes, the Li insertion potential of TiO_2 lies roughly within the stability window of common organic electrolytes, which leads to superior safety. Furthermore, anatase TiO_2 shows a very low volume change (< 4 %) during cycling, which leads to high cycling stability; a high-rate, low-temperature charge/discharge capability; and high thermal stability in both the charged and discharged state. These properties make it an excellent host structure for thin films of Si.

The theoretical capacity of TiO_2 corresponds to 1 mol of inserted Li per mole of TiO_2 (x = 1). This work described herein was targeted at making a persuasive correlation between the Si-coating thickness, morphological characteristics, and electrochemical lithium storage performance in Si-coated $SiTiO_{2-x}$-C NTs.

Nanotube morphology, structure, and chemical composition

Thin-film Si-coated anodes with different Si-coating thicknesses (5, 20, 30, 40, and 50 nm) have been synthesized and exploited as alloying anodes for next-generation, high-energy-density Li-ion batteries. Ex situ XRD measurements revealed that the different Si-coating thicknesses did not influence the lithiation characteristics of the subjacent anatase TiO_{2-x}-C nanotubes (NTs) substrate. These findings were congruent with the potential dependent diffusion coefficient obtained by using electrochemical impedance

spectroscopy and the galvanostatic intermittent titration technique. Ex situ attenuated total reflection (ATR) FTIR spectra of the Si-coated $SiTiO_{2-x}$-C NTs at 40 mV of the different Si-coating thicknesses provided information about the surface chemistry of the materials before and after lithiation. The species on the lithiated $SiTiO_{2-x}$-C NTs were identified as physisorbed or chemisorbed water and OH groups. These groups could react with Li^+ to form Li_2O, or signals could be attributed to weakly adsorbed organic molecules, such as CO_3^{2-} or COOH. Scanning electron micrographs of the pristine samples showed that at approximately 40 nm of Si-coating, the NTs were covered completely with a Si film.

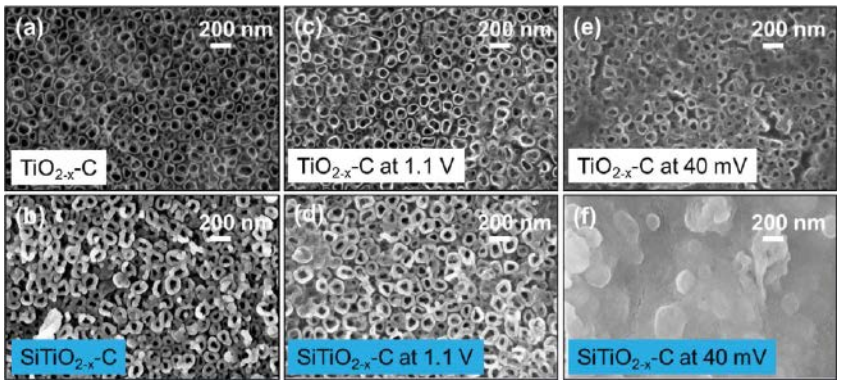

Figure 1. *SEM images of (a) TiO_{2-x}-C NTs and (b) Si-coated (10 nm) $SiTiO_{2-x}$-C NTs before contact with the electrolyte. (c) TiO_{2-x}-C NTs and (d) $SiTiO_{2-x}$-C NTs after lithiation to 1.1 V, (e) TiO_{2-x}-C NTs and (f) $SiTiO_{2-x}$-C NTs after lithiation to 40 mV.*

Microscopic characterization

To determine the active electrode anatase (TiO_2) volume and the corresponding mass fraction of the deposited Silicon scanning electron micrographs of Si-coated carbon containing anatase nanotubes ($SiTiO_{2-x}$-C NT) before and after Si deposition were observed with a CrossBeam NVision 40 from Zeiss. The micrographs were acquired using an electron-acceleration voltage of 15 kV by using the InLens detector. The TiO_{2-x}-C NTs morphology was also determined from SEM images; the NTs were characterized by a 1.1 mm average tube length, 15 nm average wall thickness at the top, 115 nm average pore diameter, and a solid hemisphere at the bottom of each tube. Analysis of the SEM cross-sections for the $SiTiO_{2-x}$-C NTs revealed that the Si coating covers approximately 160 nm of the NTs top length on both the inner and outer walls.

SEM images of anatase TiO_{2-x}-C NTs and $SiTiO_{2-x}$-C NTs with a Si coating of 10 nm after galvanostatic lithiation to different potentials are shown in Figure 1. Micrographs of TiO_{2-x}-C NTs and $SiTiO_{2-x}$ NTs before contact with the electrolyte are shown in Figure 1 a and b. Thicker NT walls were observed for $SiTiO_{2-x}$-C NTs compared to TiO_{2-x}-C NTs because of the 10 nm-thick Si coating, and the individual geometry of the NTs was still visible. There was no visible change in NT morphology for both systems after lithiation to 1.1 V (Figure 1 c and d). The SEM top view showed some minor coverage of the NTs top layer by surface deposits that were not removed fully by emersion from the battery cell and rinsing with dimethyl carbonate (DMC) after the lithiation experiment. If lithiated to 40 mV, the NT morphology of anatase TiO_{2-x}-C NTs remained unaltered, and their partial coverage by surface film deposits was observed. In contrast, the individual $SiTiO_{2-x}$-C NTs were no longer visible after lithiation to 40 mV (Figure 1 f) and were covered by a continuous film of lithiated Si because of the high volumetric expansion of Si (up to 280 %) upon lithiation.

Triton analysis and galvanostatic cycling

Triton analysis was additionally used to show the homogeneous lithiation behavior of TiO_{2-x}-C NTs and $SiTiO_{2-x}$-C NTs. Thereby, triton analysis displayed high areal Li densities of $SiTiO_{2-x}$-C NTs after lithiation to 40 mV (23.7 ± 1.0) $\mu gLicm^{-2}$ in agreement with the value determined electrochemically of (36.6 ± 4.6) $\mu gLicm^{-2}$. These lithiation characteristics were consistent for different Si-coating thicknesses and were not altered upon subsequent cycling. The results of the authors further displayed superior kinetics for the lithiation of Si over anatase in $SiTiO_{2-x}$-C NTs. Although both systems were characterized by a good cycling stability (Coulombic efficiency close to 100%), the capacities of the Si-coated $SiTiO_{2-x}$-C NTs were approximately twice as high as those reached by uncoated TiO_{2-x}-C NTs (≈ 50 vs. ≈ 25 mAh cm^{-2} after 110 cycles) because of the exceptionally high specific capacity of Si. Interestingly, for all C rates, the specific capacities reached a maximum at a Si-coating thickness of 30 nm, whereas a thick Si-coating of 50 nm led to specific capacities comparable to that of the carburized anatase reference sample without Si. It can be inferred that this maximum at 30 nm was determined mainly by the tubular geometry of the electrodes, which suggests that the resulting free volume for Si expansion upon lithiation was the limiting constraint. The expansion of Si upon lithiation normal to the electrode surface resulted in a "sweet spot" for the overall capacity of Si-coated NTs and Si-coated nanostructures in general. With the $SiTiO_{2-x}$-C NTs geometry used in this work, the sweet spot was at a Si-coating thickness of approximately 30 nm. At this Si-coating thickness, just enough Si was available to be lithiated to fill the accessible free volume and no observable structural damage occurs during the lithiation/delithiation cycle. As the free volume was an important parameter in any nanostructured material, the results of the authors suggest that such an optimum in the specific lithiation capacity was immanent to any Si-coated nanostructured electrode.

Summary

Different Si-coating thicknesses did not influence the lithiation characteristics of the subjacent anatase TiO_{2-x}-C nanotubes (NTs) substrate. Triton and electrochemical analysis revealed a homogeneous lithiation behavior of TiO_{2-x}-C NTs and $SiTiO_{2-x}$-C NTs. High areal Li densities of $SiTiO_{2-x}$-C NTs could be observed after lithiation to 40 mV. Furthermore, a good cycling stability could be measured showing the capacities of the Si-coated $SiTiO_{2-x}$-C NTs were approximately twice as high as those reached by uncoated TiO_{2-x}-C NTs. For all C rates, the specific capacities reached a maximum at a Si-coating thickness of 30 nm and the sweet spot was approximately at the same thickness.

Digest of
Auer A., Jonasson N. S. W., Apaydin D. H., Mardare A. I., Neri G., Lichtinger J., Gernhäuser R., Kunze-Liebhäuser J., Portenkirchner E.; Optimized Design Principles for Silicon-Coated Nanostructured Electrode Materials and their Application in High-Capacity Lithium-Ion Batteries; Energy Technology, 2017, 5, 2253–2264; https://doi.org/10.1002/ente.201700306.

High Resolution SEM Characterization of Nano-Precipitates in ODS Steels

Jóźwik I., Strojny-Nędza A., Chmielewski M. et al.

The performance of the present-day scanning electron microscopy (SEM) extends far beyond delivering electronic images of the surface topography. Oxide dispersion strengthened (ODS) steel is one of the most promising materials for the future nuclear fusion reactor because of its good radiation resistance, and higher operation temperature up to 750°C. The microstructure of ODS steel should not exceed tens of nm, therefore there is a strong need in a fast and reliable technique for their characterization. In this work, the results of low-kV SEM characterization of nanoprecipitates formed in the ODS matrix were presented. Application of highly sensitive photo-diode backscattered electron (PDBSE) detector SEM imaging allowed for the registration of single nm-sized precipitates in the vicinity of the ODS alloys. The composition of the precipitates was confirmed by transmission electron microscopy combined with energy dispersive X-ray spectroscopy (TEM-EDS).

Groups and types of nanoparticles

Mechanical alloying and SPS were used to produce dense, compact, oxide dispersion strengthened (ODS) ferritic steels Fe-12Cr and Fe-14Cr with 0.3%wt. Yttria (Y_2O_3) addition, together with Tungsten (W) and Titanium (Ti) incorporation. These materials were investigated by means of high resolution SEM, EDS, and EBSD techniques. Three groups of different sized nano-particles in ODS alloys were defined, based on the SEM micrographs. Group I consists of particles with a size above 100 nm that were uniform, while Group II contains particles between 50 and 100 nm that were non-uniform distributed within the steel matrix. Finally, Group III contains the smallest particles (size below 50 nm) with a predominant localization in the grain boundaries of the matrix.

Microstructure characterization

Samples of ODS steels were investigated by two high-resolution SEM including a Zeiss Auriga CrossBeam Workstation. The use of primary energy in the range of 0.5 to 10 keV was made possible by means of a highly developed advanced detection system. The combination of versatile detectors allowed for imaging with the selection of real signals from secondary electrons (SE1 and SE2) and backscatter electrons (BSE) in real time. Electron backscattered diffraction (EBSD) was used for microstructure characterization in terms of the metallic grain size and distribution. Elemental analysis of precipitates and bulk material was performed by energy dispersive X-ray spectroscopy (EDS).

EDS analysis revealed two different types of nanoparticles, namely Y free clusters containing iron (Fe), chrome (Cr) and impurity elements, and Y-O-Ti rich clusters. The results were confirmed by SEM micrographs analysis in compositional contrast mode recorded at various imaging conditions. Application of highly sensitive PDBSE detector in SEM imaging allowed for the registration of single nm-sized precipitates in the vicinity of the ODS alloys. The increase in Cr concentration gave rise to increase of the number of nano- and submicron-size precipitates. Low-kV observation in deceleration mode with a negative stage bias revealed at least two different phase compositions of the selected precipitates, which stayed in the agreement with EDS measurements.

Low kV electron imaging

By the application of of a low energy primary electron beam it was possible to record images in contrast formed between the precipitates. Semi-inlens detectors of SE1 and BSE electrons were used for that purpose. Low-voltage observations with atomic contrast were possible due to energy filtering and specific collection parameters of the electrons. Fig. 1 presents the images collected simultaneously in two channels for the same part of the sample ODS 14Cr at 1 keV.

In case of the SE1 image (Fig. 1a) the differences in the appearance of the precipitates were related to secondary electron emission intensity which may be dependent to either composition of constituent elements, crystalline state, crystal orientation, conductivity, work function and so forth. The compositional contrast between two fragments of precipitate could be clearly seen in the BSE image (Fig. 1b). Red arrows point to the part of the precipitate with higher average atomic number. Simultaneously, that part appears darker in the SE1 image. Assuming that the darkening of the precipitate in the SE1 image follows the higher content of oxygen in the analyzed volume (thus more resistant), one may presume that this part (appearing bright in the BSE image) is composed mostly of Y_2O_3.

The best example confirming such kind of explanation was the comparison and analysis of the images acquired at 0.5 keV with the stage bias. In the studied case the stage and the sample were biased with -2,000 V to obtain the primary beam of 0.5 keV in deceleration mode.

Again, the part of the precipitate composed of the lighter elements turns out as darker in the BSE image (blue arrows Fig. 2b). At the same time, it becomes intensely bright in the SE1 image, possibly due to the fact of high negative voltage applied to the sample and the stage. In fact, the composition of this precipitate could not be definitely

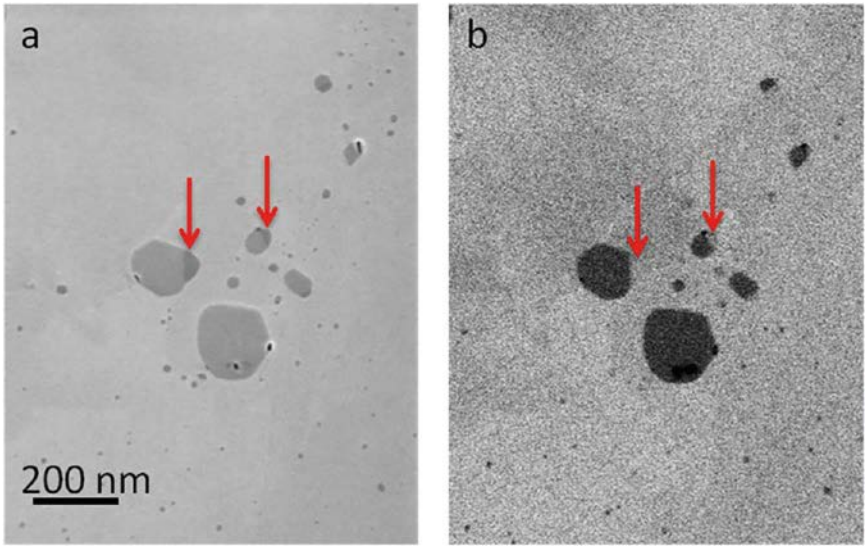

Fig. 1: SEM image of sample 14Cr in SE1 (a) and BSE (b) registered at 1 keV of primary beam energy; red arrows indicate high atomic number composition precipitates.

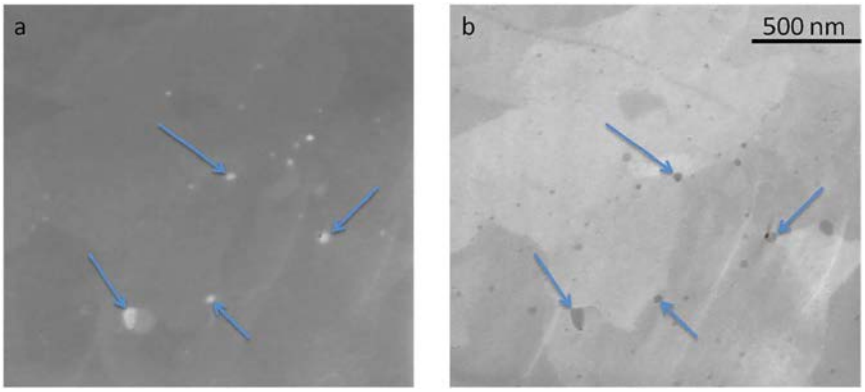

Fig. 2: SE1 (a) and BSE (b) images recorded using 0.5 keV beam in deceleration mode (stage biased to -2,000V); blue arrows indicate highly resistive/low mass precipitates in sample ODS 14Cr.

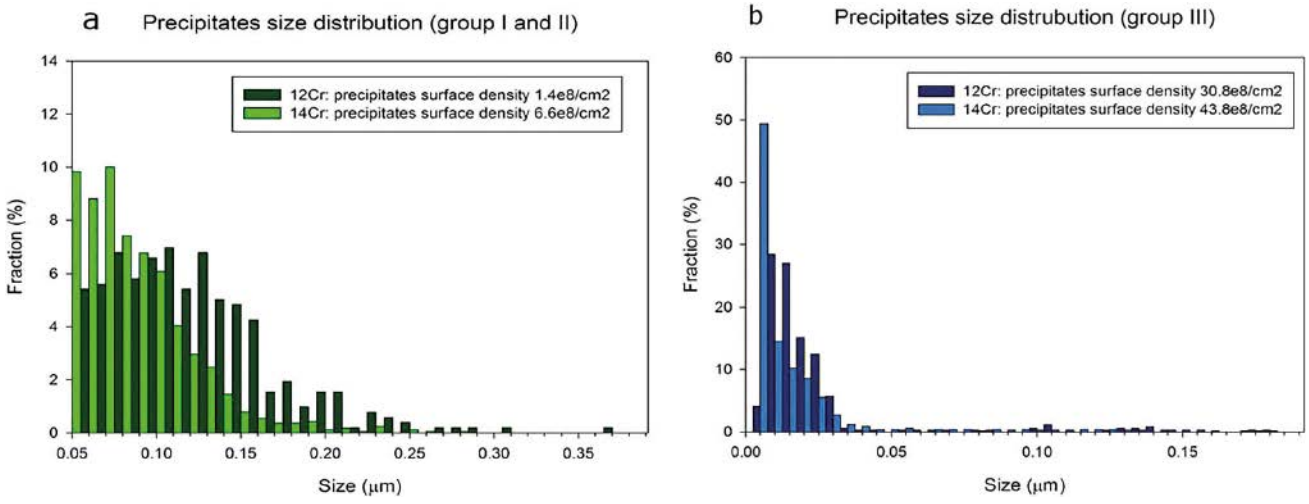

Fig. 3: Size distribution of precipitates in ODS SPS steels with different concentration of Cr: (a) group I and II precipitates (size 50–100 nm and above), (b) group III nano-precipitates (size below 50 nm).

and precisely identified, but it was certainly possible to distinguish between (at least) two types of precipitates. Assuming that the brighter parts in BSE image are related to Y_2O_3 and along with the EDS analysis the authors concluded that the Y_2O_3 nano-powders initiate the growth of the precipitates of Fe-O-Cr in the ODS steel.

Size distribution of precipitates

The size distributions of nano-precipitates obtained by automatic counting of particles belonging to certain size classes/groups are depicted in Fig. 3a–b. It was observed that the increase in the Cr incorporation, shifts the size distribution of group I and II nanoparticles towards lower values, but in turn the precipitates prevail in the number (Fig. 3a). The calculated surface density (number per area) of precipitates reached 6.6 x 10^8 cm^{-2} for the 14% Cr in comparison to 1.4 x 10^8 cm^{-2} for the 12% Cr concentration. Similarly, the nano-precipitates of group III were more numerous in case of 14% Cr comparing to 12% Cr, i.e., 43.8 x 10^8 cm^{-2} versus 30.8 x 10^8 cm^{-2}, however their distributions remained alike.

The larger submicron size precipitates (group I) observed in ODS alloys were investigated by means of the EDS technique. The very week signal of comparable value from Y was registered irrespective of the place of measurement (precipitate or steel matrix). Obtained results indicated the presence of Ti-O-Y rich precipitates (the most desirable from the point of view of the mechanical properties of ODS steel) as well as Fe-Cr-O clusters. The results were confirmed with the TEM-ESD analysis which identified the precipitates as the Ti-rich or Cr-rich phases.

This study proves that SEM becomes a complementary technique to TEM. It allows for fast and relatively easy imaging of the microstructure of ODS alloys, but with no possibility of definite determination of the precipitates phase composition, in contrast to TEM-EDS. However, the ease of operation and simple sample preparation, the possibility of large area observation (thus good statistics of the analyzed precipitates) make the HR SEM an attractive tool for ODS alloys characterization and preliminary screening.

Summary

Dense compact Fe-12Cr and Fe-14Cr alloys with 0.3 wt.% Y_2O_3 addition together with W and Ti inserts were produced and their microstructure examined by electron microscopy and EDS. Three groups of nanoparticles in ODS alloys of different sizes and two different types of nanoparticles: Y free clusters with Fe, Cr and impurity elements and Y-O-Ti rich clusters could be identified. The use of a highly sensitive PDBSE detector in SEM imaging enabled the registration of single nm-sized precipitates near the ODS alloys. The increase of the Cr concentration leads to an increase in the number of nano- and submicron-size precipitates. Low kV observation in delay mode with negative phase bias led to at least two different phase compositions of the selected precipitates, which agree with the EDS measurements.

Digest of
Jóźwik I., Strojny-Nędza A., Chmielewski M., Pietrzak K., Kurpaska Ł., Nosewicz S.; High resolution SEM characterization of nano-precipitates in ODS steels; Microscopy Research and Technique, 2018, 81, 502–508; https://doi.org/10.1002/jemt.23004.

X-Ray Nano-Computed Tomography of Electrochemical Conversion in Lithium-Ion Battery

Di Lecce D., Levchenko S., Iacoviello F. et al.

In this study, a nanometric CuO anode for lithium-ion batteries was investigated by combining electrochemical measurements and ex situ X-ray computed tomography (CT) at the nanoscale. The electrode reacted by conversion at about 1.2 and 2.4 V versus Li^+/Li during discharge and charge, respectively, to deliver a capacity ranging from 500 mAh g^{-1} to over 600 mAh g^{-1}. Three-dimensional nano-CT imaging revealed substantial reorganization of the CuO particles and precipitation of a Li^+-conducting film suitable for a possible application in the battery. A lithium-ion cell, exploiting the high capacity of the conversion process, was assembled by using a high-performance $LiNi_{0.33}Co_{0.33}Mn_{0.33}O_2$ cathode reacting at 3.9 V versus Li^+/Li. The cell was proposed as an energy-storage system with an average working voltage of about 2.5 V, specific capacity of 170 mAh $g_{cathode}^{-1}$, and efficiency exceeding 99 % with a very stable cycling.

Metal oxide anodes

Metal oxides such as CuO, NiO, and Fe_2O_3 may reversibly exchange more than 1 equivalent of lithium according to a multi-electron conversion mechanism, also called displacement, evolving within a wide potential region with remarkable specific capacity. Therefore, these oxides have been proposed as alternatives to graphite and Li-alloys for application as anodes in lithium-ion batteries (LIBs) characterized by their high capacity and low cost. However, the large voltage hysteresis between charge and discharge processes, and the modest stability of the conversion reaction owing to significant structural and volume changes, have hindered the application of these electrodes in efficient full Li-ion cells.

Recently, synthetic approaches capable of retaining structural integrity and ensuring electrode stability for nanostructured metal oxides have been developed, which has only partly mitigated the voltage hysteresis issue. Indeed, the complex-displacement reaction pathway involving massive electrode reorganization actually affects the electrochemical potential stability upon prolonged cycling and leads to capacity decay, thus limiting the practical application of metal oxide anodes.

Advanced ex and in situ measurements have promoted fundamental understanding of the structural and morphological modifications along with the effects of metal oxide composition on the conversion reaction features. Among the various investigative approaches, three-dimensional imaging at the micro- and nanoscale is assumed to shed light on the particle evolution throughout the lithium-exchange process and reveal crucial morphological parameters for electrode modelling, such as the phase volume fraction and the particle size distribution. In particular, X-ray nano-CT enables a detailed reconstruction of the spatial distribution of the various electrode components and provides useful qualitative compositional information associated with the attenuation of the incident beam. Insights into the displacement process may pave the way for improved performance by aiming at effective employment of metal oxides as anodes in efficient and stable full-cells, which is considered essential to demonstrate the applicability of this class of materials.

Scanning/transmission electron microscopy (SEM/TEM) and X-ray CT

The morphology of nanometric CuO powder was investigated by using a Zeiss EVO 40 SEM with a LaB6 thermionic gun and a Zeiss EM 910 TEM with a tungsten thermionic gun. Ex situ X-ray CT was performed on a pristine CuO sample as well as CuO samples after 1 and 10 galvanostatic cycles at 0.2 C. The Nano-CT datasets were obtained using a Zeiss Xradia 810 Ultra instrument equipped with a micro-focus rotating chrome (Cr) anode and tomographic datasets were reconstructed by the Zeiss XMReconstructor software employing a filtered back-projection algorithm. Furthermore, the pristine CuO electrode was investigated by X-ray micro-CT through a Zeiss Xradia 520 Versa instrument employing a polychromatic micro-focus source and a tungsten target. The tomographic datasets were reconstructed by the Scout-and-Scan Control System Reconstructor software (Carl Zeiss Inc.) employing a filtered back-projection algorithm.

Structure and electrochemical response of a nanomeric CuO electrode

Nanometric copper oxide (CuO) was considered for possible application as a conversion anode in Li-ion cells by using a multidisciplinary approach that advantageously combined electrochemical techniques and advanced X-ray tomography imaging. The nano-powder displayed pronounced crystallinity with a monoclinic lattice belonging to the C1c1 (9) space group (ICDD PDF #80-1916) and formed sub-micron agglomerates with size approaching 500 nm composed of nanoparticles (about 70 nm) and a few relatively large micrometric particles. Electrochemical studies showed a conversion reaction with suitable stability and remarkable charge/discharge hysteresis accompanied by a substantial structural change during operation. Furthermore, measurements in Li-ion cell revealed an increasing capacity trend

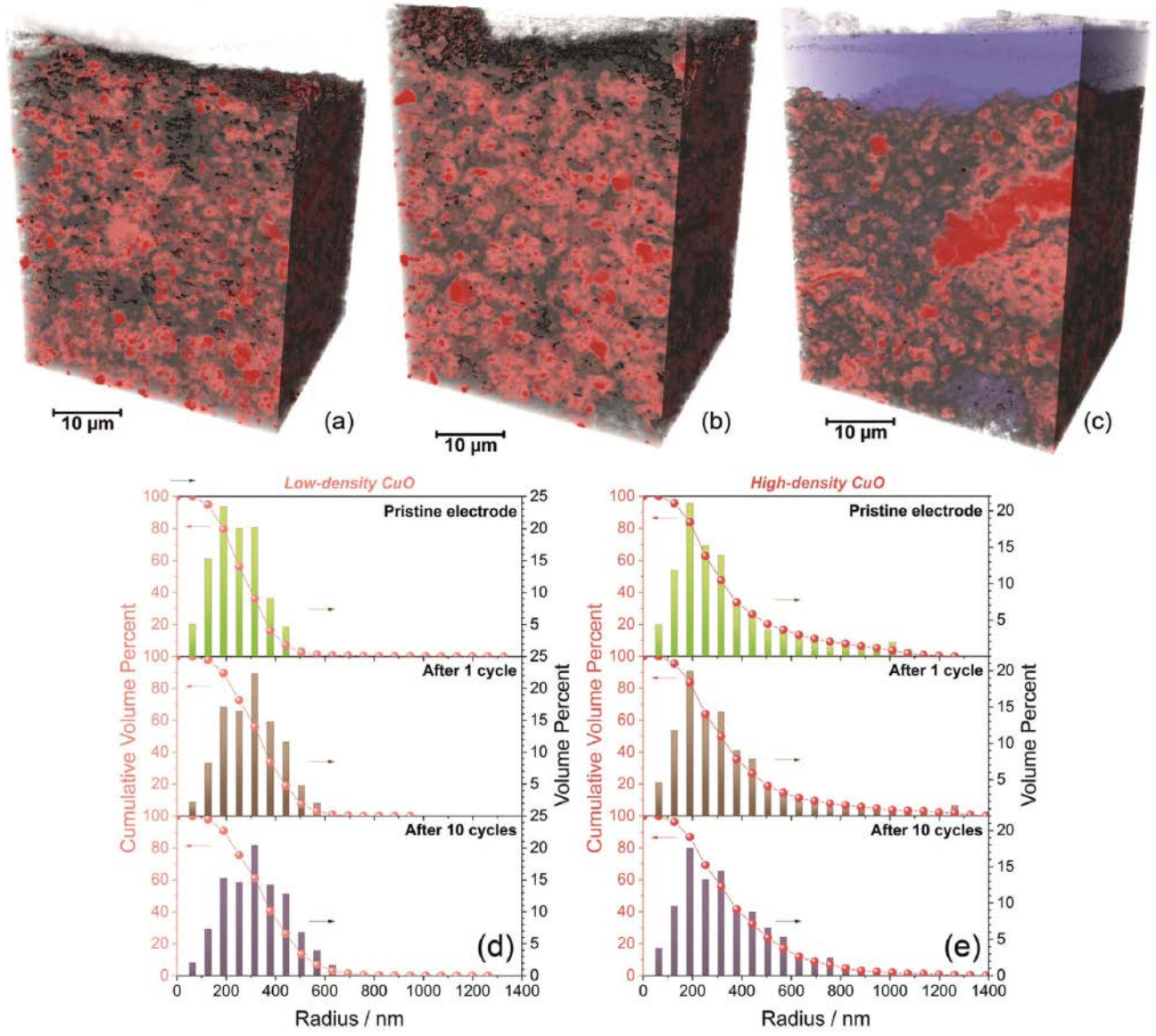

Fig. 1: Ex situ X-ray nano-CT study of the CuO electrode. (a–c) Volume rendering for (a) pristine CuO, (b) CuO after 1 cycle, and (c) CuO after 10 cycles. Voxel size : 63 x 63 x 63 nm³ ; Dataset size : 600 x 600 x 800 nm³. (d, e) Continuous particle size distribution of (d) low-density and (e) high-density CuO for a cropped dataset (600 x 600 x 600 voxel³. Microfocus rotating anode X-ray source set at 35 kV and 25 mA. Scans performed in X-ray absorption-contrast and largefield-of-view (65 µm) modes, by taking 1601 projections through 180° with 50 s exposure and 1 voxel binning.

upon cycling, which led to a partial activation of the material. Ex situ X-ray nano-computed tomography suggested a significant electrode reorganization upon cycling and gradual growth of lower density copper oxide aggregates compared to the pristine material. In agreement with the electrochemical impedance spectroscopy (EIS), SEM, and energy dispersive X-ray spectroscopy (EDS) investigations, three-dimensional reconstruction (Figure 1) of the electrode throughout cycling evidenced the precipitation of a thick solid/electrolyte interphase (SEI) after 10 cycles. A high Li^+ permeability ensured remarkable cycling behavior upon 100 cycles.

Volume rendering of the computed tomography analysis are shown in Figure 1 a–c. As mentioned above it displays the electrode evolution in the cell and suggests substantial modifications after 10 cycles attributed to the SEI growth and copper oxide agglomeration. These observations were confirmed by the continuous particle size distribution analysis of the cropped sub-volumes reported in Figure 1 d, e. The cropped sub-volumes were segmented into the following four phases: pores and exterior, SEI, carbon-binder domain, and copper oxide, by employing a grayscale threshold method. Furthermore, two CuO domains

having low and high density were identified according to the grayscale histograms.

The cropped sub-volumes datasets reveal a growth of copper oxide aggregates with estimated radii ranging from 300 to 700 nm, as well as a decrease in the number of particles smaller than 300 nm. Such changes were observed for both copper oxide domains, alongside with a decrease in the number of high-density CuO particles larger than 800 nm.

High capacity of nanometric CuO

Indeed, the nanometric CuO delivered high capacity with a maximum value exceeding 600 mAh g^{-1} after the activation, ascribed to the beneficial effect of the electrode rearrangements. This suggested the suitability of the material for use in full-cells, which were prepared and studied. Particularly, a CuO/$LiNi_{0.33}Co_{0.33}Mn_{0.33}O_2$ lithium-ion battery, assembled by carefully tuning the electrode masses, the areal capacity ratio of negative to positive electrodes (N/P ratio), and the voltage limits stably delivered a capacity of about 170 mAh g^{-1} with respect to the cathode weight, with an average voltage of about 2.5 V. Therefore, the cell was characterized as having an energy density of about 425 Wh kg^{-1} with respect to the cathode, which may actually be reflected into a practical energy approaching that of commercial batteries based on graphite anode and layered oxide cathode. Although the issues hindering the application of conversion anodes were still not fully addressed, the presented results suggest a large room for improvement of nanometric transition metal oxide anodes. Moreover, this work highlighted that a suitable combination of X-ray CT study supported by SEM-EDS, and electrochemical characterization through voltammetry, impedance spectroscopy, and galvanostatic cycling can effectively elucidate the structural reorganization within the electrode and the evolution of the SEI upon the electrochemical process. Therefore, such an interdisciplinary method may actually provide a deep understanding of the behavior of electrode materials in LIBs.

Summary

Nanometric copper oxide showed a pronounced crystallinity and formed submicron agglomerates with a size of approximately 500 nm. Electrochemical studies showed a conversion reaction with suitable stability and remarkable charge/discharge hysteresis. Ex-situ X-ray nano-CT showed significant electrode reorganization during the cycle and gradual growth of copper oxide aggregates with lower density compared to the original material. In accordance with EIS, SEM and EDS, the three-dimensional reconstruction of the electrode during the cycle showed the precipitation of a thick SEI after 10 cycles. The nanometric CuO provided a high capacity with a maximum value of more than 600 mAh g^{-1} due to the positive effect of electrode rearrangements. The use of this material in a CuO/$LiNi_{0.33}Co_{0.33}Mn_{0.33}O_2$ lithium-ion battery provided a stable capacitance of approximately 170 mAh g^{-1} based on the cathode weight at an average voltage of approximately 2.5 V. The capacitance of this material was not affected by the electrode shift. An energy density of about 425 Wh kg^{-1} was determined for the cell, which is similar to that of commercially available batteries based on graphite anode and layered oxide cathode.

Digest of
Di Lecce D., Levchenko S., Iacoviello F., Brett D. J. L., Shearing P. R., Hassoun J.; X-ray Nano-computed Tomography of Electrochemical Conversion in Lithium-ion Battery; ChemSusChem, 2019, 12, 3550; https://doi.org/10.1002/cssc.201901123.

Evidence of Multimicrometric Coherent γ′ Precipitates in a Hot-Forged γ-γ′ Nickel-Based Superalloy

Charpagne M.-A., Vennéguès P., Billot T. et al.

This paper demonstrated the existence of large γ′ precipitates (several micrometres in diameter) that are coherent with their surrounding matrix grain in a commercial γ–γ′ nickel-based superalloy. The use of combined energy dispersive X-ray spectrometry and electron backscattered diffraction (EBSD) analysis made it possible to monitor this surprising feature, which was then confirmed by transmission electron microscopy (TEM). Coherency for such large second-phase particles was supported by a very low crystal lattice misfit between the two phases, which was confirmed by X-ray diffractograms and TEM selected area electron diffraction patterns. This configuration is believed to be the result of a dynamic recrystallization process.

Dynamic recrystallization

As in many materials with low stacking fault energy, the main softening mechanism during forging at high temperature is discontinuous dynamic recrystallization. This mechanism generally occurs with preferential nucleation on the grain boundaries of the deformed matrix. The latter is then being consumed by the growth of the newly formed grains of low energy and by nucleation that keeps generating new grains. In the case of sub-solvus forging, large γ′ particles usually pin the migrating boundaries and thus limit grain growth to a size which is determined by the distribution of second-phase particles, according to the Smith-Zener model. Under particular circumstances, the driving force associated with the difference in stored energy between the growing grains and the matrix can be large enough that the pinning forces can be overcome, and some grains can then reach much larger sizes. In the latter exceptional case, some intragranular primary γ′ particles could be observed, although most of them were located at grain boundaries and triple junctions. In both latter cases, primary precipitates had no particular orientation relationship to the surrounding matrix grain(s).

EDS/EBSD analysis

Mirror polished samples were characterized using a combined energy dispersive X-ray spectrometry/electron back-scattered diffraction (EDS/EBSD) fast acquisition speed system mounted on a high-resolution scanning electron microscope (SEM), Zeiss Supra 40, equipped with a field emission gun (FEG). The EDS/EBSD system is a QUANTAX system from Bruker, including an EDS XFlash 5030 detector and an e⁻Flash^{HR} EBSD detector, controlled by the ESPRIT software package.

The microstructure of a forged sample of René 65^{TM} has been analyzed using the above-mentioned EDS/EBSD technique (Figure 1B–D) and imaged using a back-scattered electrons (BSE) detector (Figure 1A). Compared with the BSE image (Figure 1A) the localization and shape of γ′ precipitates on the phase map (Figure 1B) corresponds well. In Figure 1B, the simultaneous representation of phases and grain boundaries shows that some primary γ′ precipitates are located inside γ grains. Because they are supposed to pin boundaries during thermomechanical processing, they are usually expected to be on grain boundaries or at triple junctions. Three typical examples of intragranular primary γ′ precipitates are arrowed in Figure 1B. One important characteristic of this configuration is that only one precipitate is contained per matrix grain.

The comparison between the phase map of Figure 1B and the orientation color-coded map of Figure 1C reveals a specific orientation relationship between those precipitates and their surrounding matrix grain. Invisible on Figure 1C, they have obviously the same orientation as the surrounding grain, within the EBSD angular resolution (typically 0.5°). Figure 1D is colored according to the kernel average misorientation value. The kernel average misorientation parameter is efficient for revealing subboundaries and interfaces with very low misorientation angles. Here, the trace of γ′ precipitates inside matrix grains is hardly visible on the kernel average misorientation map. In those coherent precipitates, even defects such as annealing twins are extended to the matrix grain. The main kernel average misorientation contrast arises either from differences in the orientation of the grains themselves which lead to slight variations in the pattern indexation accuracy, or from lattice distortions associated with the presence of dislocations in few not recrystallized grains (e.g. the one at the bottom right).

Surprising γ–γ′ configuration

The EDS/EBSD coupling technique has enabled the researchers to reveal an unusual γ–γ′ configuration in a hot-forged recrystallized microstructure of René 65^{TM} alloy. About half of the large primary γ′ precipitates are surrounded by a matrix grain with the same crystallographic orientation (Figure 1). This was confirmed by complementary TEM observations. Although the secondary and tertiary precipitates are generally coherent with their hosting grain, such configuration has not been reported yet for primary precipitates.

Studies dedicated to the evolution of growing γ′ particles during ageing treatments have shown that the critical size at which the particles become incoherent depends on the γ–γ′ lattice mismatch. In the case of a very low constrained lattice mismatch (typically $E < 0.05\%$), growing precip-

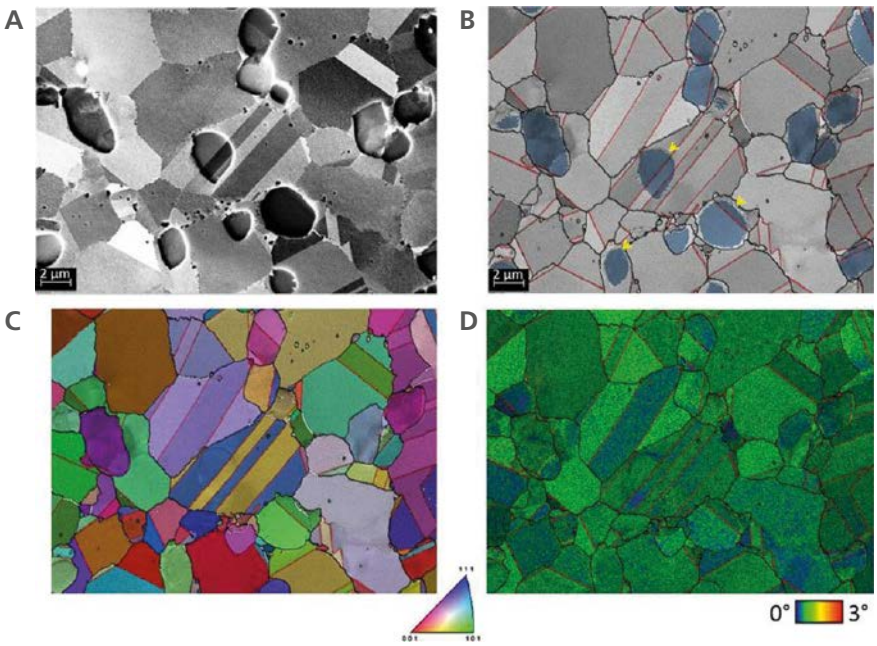

Figure 1. *Microstructure of the as-received René 65TM sample. (A) BSE image and (B) γ′ phase map (in light blue) obtained from postprocessing of EDS/DEBSD data, superimposed on the Kikuchi Pattern Quality map. (C) Orientation color-coded map (normal direction to the scanned section projected into the standard triangle) of both phases superimposed on the Kikuchi Pattern Quality map. (D) Kernel average misorientation map (average misorientation angle between each pixel and its first neighbours, excluding disorientations higher than 3°). On (B), (C) and (D), low angle grain boundaries (3–10°) are drawn white, high-angle grain boundaries black (>10°) and twins (60° around <111> with a tolerance of 5°) in red.*

itates can remain coherent until they reach a diameter of 0.5–0.7 µm.

The lattice mismatch at room temperature is too low to be measured by X-rays diffraction (XRD), both phases appear to have lattice parameters with overlapping uncertainty ranges. From those values, the lattice mismatch ε can only be estimated to be below 0.8%. The constrained lattice mismatch of similar alloys is well documented in the literature. Alloys such as IN 100, RR2000, MAR M 002 DS, SRR 99, exhibit lattice misfits at room temperature of 0.65%, 0.79%, 0.55% and 0.59%, respectively. The Nimonics group possesses lower misfits: Nimonic 115: 0.18%, Nimonic 90: 0.34%. Finally, Nimonic 105 and Udimet can be distinguished, their lattice misfit almost reaching the zero-value: 0.03% or 0.04% for Nimonics 105 and E <0.02% in Udimet 720. René 65™ belongs to the last group, as well as the powder metallurgy René 88DT from which it has been derived. René 65 and René 88DT alloys have very close chemical compositions and the lattice mismatch of René 88DT has indeed been already settled as especially low, with a constrained lattice mismatch around or below 0.05% to 0.06%. Such extremely low values are in accordance with the results obtained from XRD measurements.

Since the observed microstructure has developed during processing at high temperature, the effect of thermal expansion must be taken into account. Previous studies have emphasized the temperature dependence of the lattice mismatch in various γ–γ′ alloys, in the range of 25–1000°C and showed that the matrix expands to a greater extent than the γ′ precipitates. As a consequence, alloys exhibiting a low but positive lattice mismatch at room temperature may reach a close-to-zero, or even negative, lattice misfit at higher temperatures.

For supporting the existence of multi micrometric coherent precipitates, the lattice misfit must be close to zero (a rough estimation of the constrained mismatch allowing such large coherent structures, by balancing the contributions of the interfacial energy and the elastic strain energy, leads to E 0.03% for 5 µm coherent precipitates), which is consistent with the very low positive value measured at room temperature in the René 65™ alloy, and with the lattice misfit tending to decrease with increasing temperature. Even though, the lattice misfit may not be the factor triggering the formation of the observed coherent structures during forging of René 65™, its contribution appears to be essential for allowing their stability.

Further investigations are required for determining the formation mechanisms: does the precipitate grow coherently in the hosting grain up to the observed sizes, or does the surrounding grain develop coherently around a preexisting primary precipitate by some specific recrystallization mechanism? Later publications by the authors have proven the second hypothesis to be right.

Summary

EDS/EBSD coupling has proved to be a suitable tool for discriminating γ and γ′ phases in the René 65™ alloy. It enables the simultaneous study of phase topology as well as the possible orientation relationships, with a spatial resolution of the γ′ precipitates of about 0.5 µm under the applied experimental conditions.

In the studied forged material, about half of the primary precipitates appeared to be intragranular and coherent with their surrounding matrix grain. In those large coherent precipitates, twins are extended from one phase to the other. The other half is made of incoherent particles with similar sizes, but located on grain boundaries and triple junctions.

A close-to-zero lattice mismatch is a key factor for the stability of such wide γ–γ′ coherent interfaces. The lattice mismatch could indeed be evaluated as lower than 0.8% at room temperature, and is known to decrease with increasing temperature.

Digest of
Charpagne M.-A., Vennéguès P., Billot T., Franchet J.-M., Bozzolo N.;
Evidence of multimicrometric coherent γ′ precipitates in a hotforged γ–γ′ nickel-based superalloy; Journal of Microscopy, 2016 Royal Microscopical Society, 263, 106-112; https://doi.org/10.1111/jmi.12380.

Improved Interfaces of Mechanically Modified Lithium Electrodes with Solid Polymer Electrolytes

Liebenau D., Jalkanen K., Schmohl S. et al.

The combination of mechanically modified lithium electrodes and solid polymer electrolytes (SPEs) was investigated in the present study. So far, modified lithium electrodes, e.g., via structuring, were successfully used in combination with liquid electrolytes like ionic liquid-based and organic solvent-based ones. Specific SPEs have proven to be well compatible with lithium metal, even better than with liquid electrolytes. Nevertheless, the interface between lithium and SPEs is a complex issue. A new method for coating lithium electrode surfaces, especially structured lithium surfaces, with a solid polymer was developed to improve the interfacial properties, and thus battery performance. The wetting of the micropatterned lithium surface by the SPE and the directed lithium electrodeposition in the patterns were verified by scanning electron microscopy analysis. The electrochemical properties of Li|SPE assemblies were investigated on the basis of constant current cycling and impedance experiments.

Bottleneck high surface area lithium

Lithium is a very promising anode material for high energy density batteries. Many efforts have been taken to combine lithium metal with high capacity cathode materials, e.g., sulfur and oxygen (air), to achieve reversible cell chemistries. The research on such battery cell systems is motivated especially by the high theoretical specific capacity (3860 mAh g^{-1}) and the low density (0.53 g cm^{-3}) of lithium, which qualifies lithium particularly for portable devices. Furthermore, lithium metal features the lowest electrode potential (–3.04 V vs standard hydrogen electrode), which enables high cell voltages and high specific energies. Unfortunately, there are enormous challenges, like the inhomogeneous electrodeposition of lithium metal, leading to high surface area lithium (HSAL). To counteract these challenges of the lithium metal anode in rechargeable batteries, various approaches, such as chemical and mechanical modifications of the lithium metal, artificial solid electrolyte interphases (SEIs) as protecting layers, or gel-type, polymeric- and ceramic-based electrolytes, have been studied. The aim of these approaches is to enable homogenous electrodeposition of lithium and thus to avoid HSAL.

Microanalysis

For the scanning electron microscopy (SEM) characterization, a Carl Zeiss Auriga Modular Crossbeam workstation was used. A Schottky field emission gun with a Gemini column was utilized as the electron source. Selected micrographs were recorded with an Everhart–Thornley type detector (SE2). Particle composition were analyzed by energy dispersive X-ray spectroscopy (EDS) elemental mapping using a X-Max detector from Oxford Instruments on a Zeiss Auriga SEM.

Surface enlargement and new drop-coating technique

Lithium electrodes were fabricated using a block press and an increase in surface area of 56% compared to pristine smooth lithium metal (Li_p) was achieved. The effect of the modification in combination with only a magneto-elasto-electroporation (MEEP) membrane as the SPE (molar ratio MEEP/bis(oxalato)borate (LiBOB)/benzophenone: 1.00/0.15/0.23) was investigated by lithium electrodeposition/-dissolution experiments in Li|SPE|Li-symmetrical cells at 60 °C. The 56% surface enlargement modification ($Li_{+56\%}$) showed 45% lower overvoltages with 55 mV and 69% lower impedance with 669 Ω compared to Li_p.

Even though a decrease of the overvoltage and the impedance was observed with micropatterned lithium, the complete wetting of the structured lithium electrode surface area by the SPE needed to be ensured. Therefore, the authors presented a drop-coating technique, which allows an improved interfacial contact between the SPE and the patterned lithium electrode by filling the structures with the electrolyte and ensuring a complete wetting of the Li|SPE assembly. Prior to the drop-coating procedure, the uncured polymer was mixed with the conductive salt LiBOB and with benzophenone as cross-linking agent, and then dissolved in tetrahydrofuran (THF). This mixture was applied dropwise on the mechanically "micropatterned" modified lithium foil, which resulted in the wetting of the lithium surface area including a filling of the micropatterns, as shown in Figure 1. After evaporation of the solvent, the polymer was cross-linked directly on the electrode. It was noticed that the intrinsic properties, like the ionic conductivity, were not influenced by the variation of the preparation method.

Appropriate filled micropatterns

The successful wetting of $Li_{+56\%}$ electrodes was proven by SEM and EDS. Cross-sectional micrographs of drop-coated lithium electrodes cycled at current densities: 0.01, 0.025, 0.05, and 0.1 mA cm^{-2} each for ten cycles, are presented in Figures 2. The EDS data confirmed that nitrogen (as part of MEEP), boron (from LiBOB), and carbon (contained in MEEP and LiBOB) could be found in the micropatterning, which suggested a filling with the SPE. The SEM images of the cycled electrodes reversing the polarity every hour and 2 h at open cir-

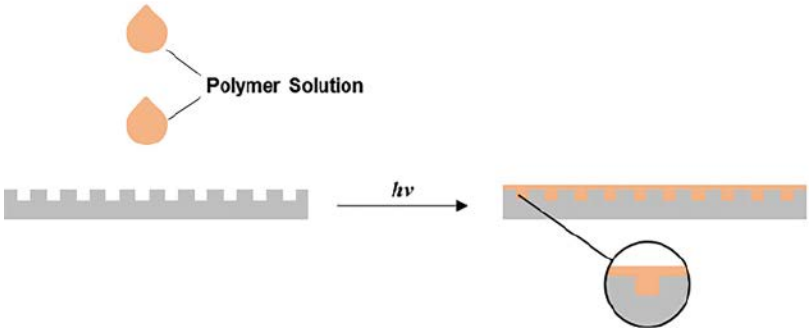

Fig. 1: Wetting of $Li_{+56\%}$ foil by application of the drop-coating method creating a well-wetted Li|SPE assembly.

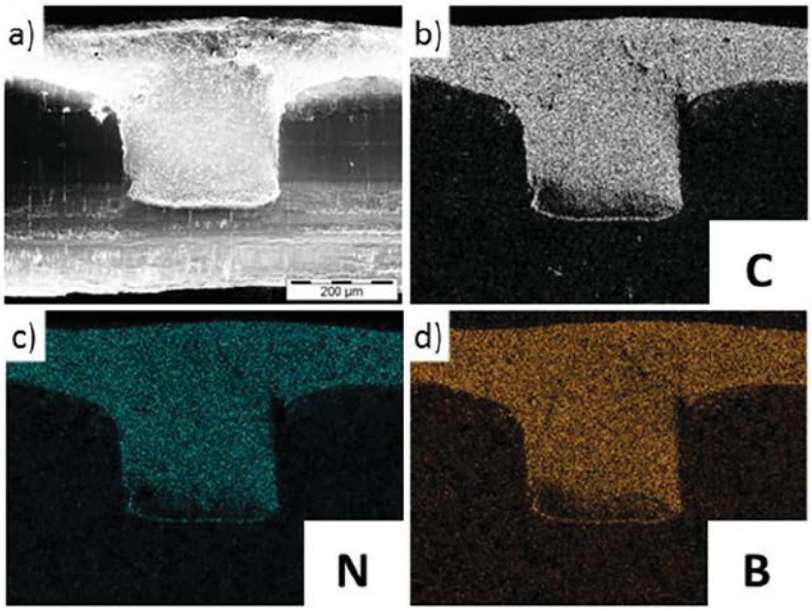

Fig. 2: a) SEM image of the cross-section (side view) of a drop-coated $Li_{+56\%}$ electrode cycled at 0.01, 0.025, 0.05, and 0.1 mA cm^{-2} each for 10 cycles and EDS analyses for b) carbon, c) nitrogen, and d) boron.

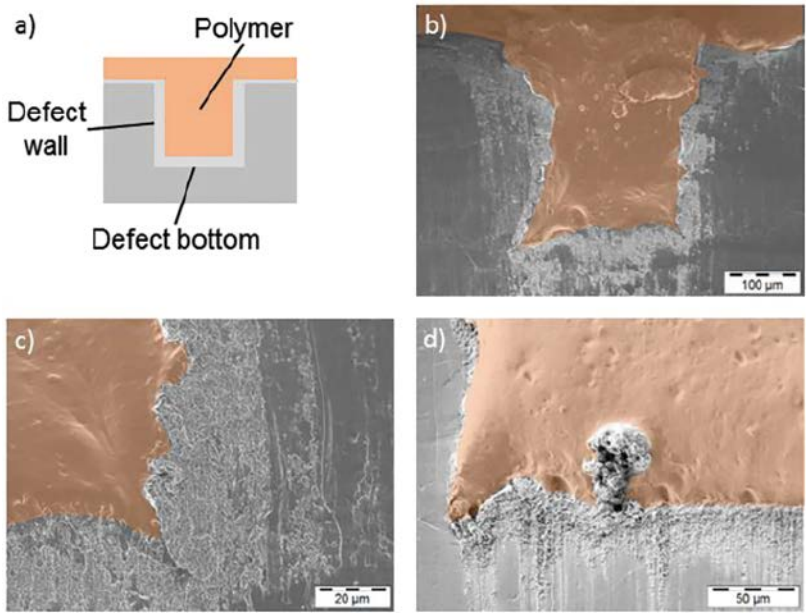

Fig. 3: a) Schematic explanation of the locality in the micropattern.
b–d) SEM images of cross-sections (side views) of long-term cycled $Li_{+56\%}$ electrodes drop-coated with the SPE MEEP (+ 15 mol% LiBOB + 23 mol% benzophenone, orange dyed) cycled at a current density of 0.1 mA cm^{-2} at 60 °C. Images of dense depositions at walls and bottoms of the micropattern at b) 200× and c) 500× magnification and d) mossy-like deposition at the bottom of a micropattern (SE2-detector, Everhart–Thornley type, topographic) at 500× magnification.

cuit voltage between the different current densities) showed that the micropatterns are still filled with SPE, and, moreover, within the short cycling time (80 h), no HSAL growth could be observed.

As a result of the analyses for $Li_{+56\%}$ electrodes employing the SPE with and without drop coating, it could be assumed that not only the increased surface area, but also the better wetting of the micropatterns leads to lower overvoltages and impedances.

Long-term cycling

Long-term constant current cycling experiments of symmetrical, drop-coated Lip and $Li_{+56\%}$ Li|SPE assemblies at 60 °C were performed at a current density of 0.1 mA cm^{-2}. The overvoltages of these cells in case of the Lip electrodes reached the set voltage limit of ± 1.5 V just after a few cycles, and a short circuit of the cell occurred after ≈570 h, while the overvoltages of $Li_{+56\%}$ electrodes occurred constantly to be under ± 0.5 V for more than 600 h (= 300 cycles).

A slight increase (50% in 600 h) in overvoltage observed after 600 h may be explained with the electrodeposition of lithium inside the patterns. These deposits either generated higher impedances as they generated additional SEI films or based on irreversible lithium deposits inside the micropatterns, which reduced the overall surface area. These findings correlated with the evolution of HSAL during long-term cycling, which was investigated by cross-sectional SE microscopy of $Li_{+56\%}$ electrodes (Figure 3). These electrodes have been imaged after 600 h electrodeposition/-dissolution cycling. The micrographs revealed that the morphology of the lithium at the walls and the bottom of the micropatterns (Figure 3a) had changed. Compared to the pristine lithium, the lithium deposits had now a rather porous morphology. These structural differences were the result of the successively repeated electrodissolution and electrodeposition of lithium during cycling (Figure 3b,c). Partial moss-like HSAL formation was observed at the bottom of the micropatterns that grew into the SPE and shifted it upwards (Figure 3d). Moreover, the lithium electrodeposition resulted in primarily dense, homogenous deposition on the electrode surface especially at the edges of the micropatterns.

As a result, an effective wetting of micropatterned lithium metal electrodes with SPE was achieved while lithium growth occurred on the surface of the electrode. This growth was especially distinctive at the walls and the bottom of the patterns as illustrated in Figure 3a. However, the formation of inhomogeneous high surface area lithium was suppressed which increased the safety of the lithium metal anode.

Summary

The combination of SPEs with mechanically "micropatterned" modified lithium electrodes was investigated. A significant decrease of overvoltages and impedances in symmetrical Li||Li cells due to the lower current density was observed. The micropatterning was produced by block pressing and with the drop-coating method, a new way to assure an effective wetting of the mechanically created structures was introduced. This was subsequently proven by SEM and EDS analyses for pristine as well as for cycled electrodes. Moreover, the long-term cycling experiments in symmetrical Li||Li cells revealed that micropatterning combined with the SPE led to a longer cycle life and a higher cycling stability for the presented system at 0.1 mA cm^{-2} and 60 °C. In SEM investigations of cycled electrodes, a homogenously distributed electrodeposition of lithium in the micropatterns could be observed. Nevertheless, small amounts of HSAL, partially penetrating the SPE, were found very occasionally on the lithium surface. Overall, the here presented combination of mechanically modified electrodes and SPEs led to longer cycle life due to improved interfacial contact. Insufficiently coated interfaces of SPEs and lithium anodes were assumed to play a crucial role for the failure mechanisms of lithium metal batteries based on solid electrolytes. Because of the simplicity of the drop-coating method, the transfer of this method to other polymer-based electrolytes and both mechanically modified and nonmodified lithium surfaces was recommended to ensure effective wetting.

Digest of
Liebenau D., Jalkanen K., Schmohl S., Stan M. C., Bieker P., Wiemhöfer H.-D., Winter M., Kolek M.; Improved Interfaces of Mechanically Modified Lithium Electrodes with Solid Polymer Electrolytes; Advanced Materials Interfaces, 2019, 6, 1900518; https://doi.org/10.1002/admi.201900518.

Size Effects on the Mechanical Properties of Nanoporous Graphene Networks

Tang D.-M., Ren C.-L., Zhang L. et al.

It is essential to understand the size scaling effects on the mechanical properties of graphene networks to realize the potential mechanical applications of graphene assemblies. In the present paper, a "highly dense-yet-nanoporous graphene monolith (HPGM)" was used as a model material of graphene networks to investigate the dependence of mechanical properties on the intrinsic interplanar interactions and the extrinsic specimen size effects. The interactions between graphene sheets could be enhanced by heat treatment and the plastic HPGM was transformed into a highly elastic network. A strong size effect was revealed by in situ compression of micro- and nanopillars inside electron microscopes. Both the modulus and strength were drastically increased as the specimen size reduced to ≈100 nm, because of the reduced weak links in a small volume. Molecular dynamics (MD) simulations revealed the deformation mechanism involving slip-stick sliding, bending, buckling of graphene sheets, collapsing, and densification of graphene cells. In addition, a size-dependent brittle-to-ductile transition of the HPGM nanopillars was discovered and understood by the competition between volumetric deformation energy and critical dilation energy.

High-density porous carbon-based materials

Carbon nanomaterials are crucial for mechanical applications, such as microelectromechanical systems (MEMS) and nanoelectromechanical systems (NEMS), sensors, and structural composite materials because of the extremely strong carbon–carbon bonds, as demonstrated by the ultimately high stiffness and strength of individual sp^2-bonded graphene, carbon nanotubes, and sp^3-bonded diamond nanowires. A theoretical simulation on the 3D graphene cellular assemblies predicted that their specific strength is potentially much higher than that of steel, at a relatively high density.

Furthermore, high-density porous carbon-based materials have demonstrated superior performance in energy storage devices, such as supercapacitors with high volumetric capacitance, Li-ion batteries, and Li–S batteries with high volumetric energy density.

Fabrication and analysis of micro- and nanopillars

A mechanically polished sample was used to fabricate nano- and micrometer size pillars via focused ion beam (FIB) (Zeiss Auriga dual beam FIB or JEOL JIB-4000). For in situ tests in SEM, micropillars were milled out directly on the polished bulk sample.

In situ nanoindentation and compression tests in SEM (Zeiss Auriga) were carried out using a comprehensive in-situ nanomechanical testing system for SEM and FIB/SEM from Bruker with a cube corner indenter and a flat indenter, respectively.

Transition from flexible to rigid networks

Due to the highly anisotropic structure of the HPGM graphene sheet with strong covalent bonding in the plane and van der Waals forces between the planes, the cellular boundaries within a continuous graphene sheet were expected to be strongly linked. And those pores composed of different graphene sheets were expected to have weak links. After heat treatment at 1600 °C, the nanoporous structure of HPGM-HT was well kept, and the atomic structure became more ordered. It was also found that rounded pores were transformed into polyhedral shapes, which also indicated the reconstruction of graphitic planes. Because of the enhancement of crystalline structure and interactions between the graphitic planes, the flexible network of the HPGM-RT was transformed into a rigid network of the HPGM-HT.

Transition from high plasticity to high elasticity

Nanoindentation experiments at different loading and depth have been conducted for both HPGM-RT and HPGM-HT. It was observed that both the modulus and hardness were decreased along with the increase in penetrating depth and contact volume, indicating a size effect on mechanical properties. The indentation process was observed by in situ SEM imaging, as demonstrated in Figure 1. The plastic deformation of HPGM-RT and elastic recovery of HPGM-HT were well captured by SEM images before and after indentation. While a triangular imprint was left on the surface of HPGM-RT under loading to 10 mN (Figure 1b), only a slight trace was detected after the indentation for HPGM-HT, even when the load was 30 mN. Under a load of 30 mN, the plastic deformation for the HPGM-RT was ≈65%. In contrast, HPGM-HT could recover elastically to ≈92% even under a load of 80 mN. The change in mechanical behaviors was consistent with the alteration of microstructures. After high temperature treatment, the interactions between graphene planes and, in turn, the crystalline order were enhanced. As a result of the enhanced rigidity, easy interplanar sliding was restricted, and HPGM was transformed from a flexible network with high plasticity to a highly elastic network.

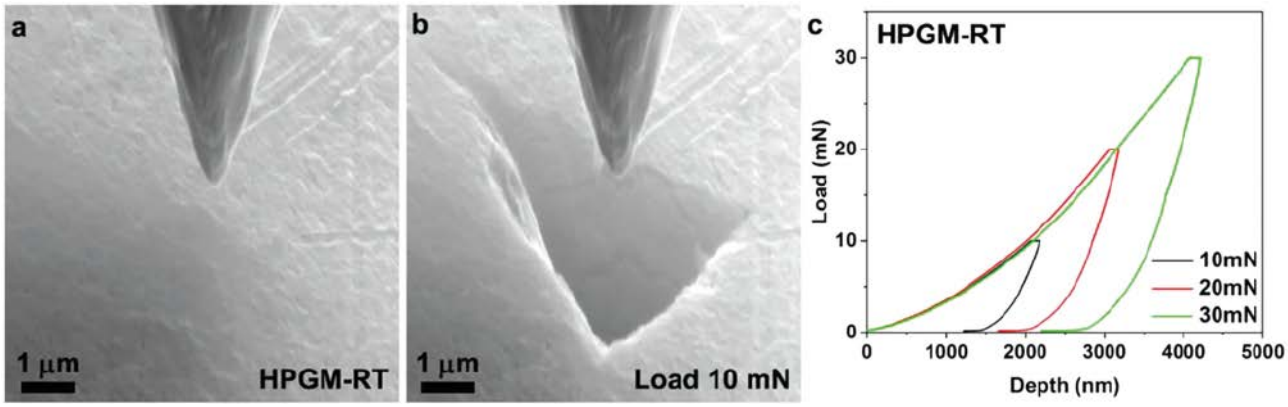

Fig. 1: Mechanical characterizations of bulk HPGM by in situ SEM nanoindentation. a, b) SEM images of HPGM-RT before and after nanoindentation under a load of 10 mN. c) Load-displacement curves of HPGM-RT with the loads limited at 10, 20, and 30 mN, revealing a plastic deformation.

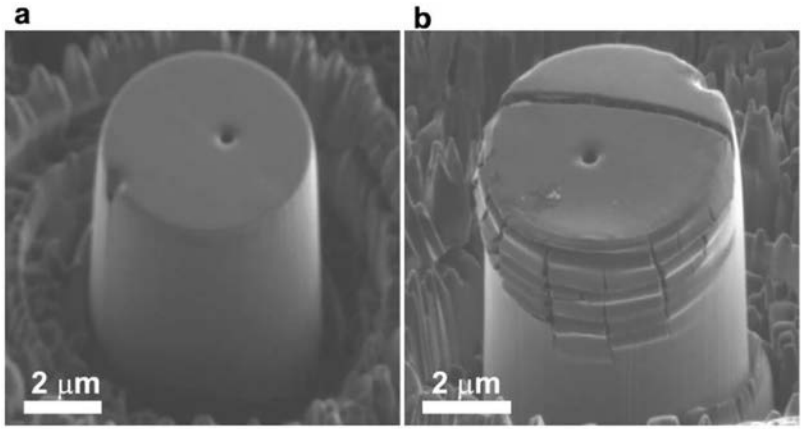

Fig. 2: Mechanical properties of HPGM micro- and nanopillars. a, b) SEM images before and after a compression test on a HPGM-RT micropillar. The side surface shows a periodic buckling feature, with multiple cracks detected both at the top and side portions.

Size effects on compressive properties

In order to investigate the size effects on the compressive properties of HPGMs, micro- and nanopillars with diameters from ≈100 nm to ≈5 μm were analyzed. SEM images of a HPGM-RT micropillar before and after compression are shown in Figure 3a, b. The pillar has a diameter of 4.1 μm and a height of 8.0 μm. Multiple yielding-cracking events were detected with the first yield at a stress of 156.5 MPa and a strain of 8.6%. The pillar was continuously compressed revealing a stress plateau at ≈205 MPa, until the retraction of the indenter at a strain of 58.0%. After unloading, a plastic deformation of 40.9% was recorded, corresponding to ≈70.5% of the maximum strain. The SEM image after compression showed multiple cracks initialized from the top and side portions. An interesting waving morphology was observed as a result of layer-by-layer buckling. Therefore, even though cracks were initiated and propagated, no catastrophic failure was observed, indicating that stress concentration at the crack tips could be effectively dissipated through the highly curved and interlinked flexible graphitic network.

Furthermore, by reducing the sample size from a micrometer to the nanometer range, which was achieved by reducing weak points in the network, it could be determined that both the modulus and the strength were drastically increased and at the same time a brittle ductile transition was achieved.

The study pointed out that the moduli of the nanopillars could be as high as ≈33 GPa, close to C_{33} of graphite crystals, corresponding to the compression between the graphitic layers, which indicated that the interlayer sliding mode was restricted in the nanoscale HPGM.

Structural model

The mechanical properties of bulk HPGM-RT described here, such as modulus, hardness, and strength, were close to the compactly packed graphene monoliths, consistent with the general density-dominated scaling law. However, a strong size effect was discovered for the HPGM nanopillars, with a remarkable combination of a high strength around 1.7 GPa and a ductility of ≈15%.

The mechanical properties and size effects of HPGM could be understood via

analyzing a network model including weak and strong links: Micrometer scale graphene sheets were stacked and assembled into a nanoporous structure. The crystalline order determined the interaction between the graphene planes and the network rigidity. The interactions between the graphene sheets could be tuned by heat treatment; as a result, the modulus of HPGM-HT was notably enhanced compared with that of HPGM-RT. In addition, there were two types of links connecting the cells. If the neighboring cells were connected by an extended graphene sheet, a strong link of covalent bonding was expected. Otherwise, only a weak link of van der Waals forces existed. The number of weak links was proportional to the sample volume. The reduced weak links could explain the enhanced strength of the HPGM nanopillars.

Molecular dynamics

MD simulations have been carried out to understand the atomic deformation mechanism of HPGM. An ideal model of orderly packed graphene assembly was constructed to uncover the deformation mechanism. In addition, a randomly packed graphene assembly, closely modeling the experimental structure, was built to get an insight into the deformation processes. The compression process of an orderly packed unit was featured by sequential sliding, bending, buckling, and densification as the compressive stress and strain were increased. Under compression, sliding bending was observed for the weakly linked graphene sheets and buckling was observed for the strongly linked sheets.

In this report, the weak links in the graphene networks was considered as microcracks. As the size decreased, the required stress for propagating cracks increased, until reaching a level to activate the buckling of the cells, leading to the brittle-to-ductile transition. Currently, the mechanical performance of HPGM at larger and bulk scales was limited by the weak links in the larger volume. Therefore, the key for practical mechanical applications is to control the number and distribution of weak links. Possible strategies include transforming the weak van der Waals forces into strong covalent bonding and introducing heteroions or functional groups as bridges between graphitic sheets to fabricate graphene enhanced composite materials.

Summary

The mechanical properties of nanoporous graphene networks were investigated at multiple length scales by nanoindentation and in situ SEM compression, with an emphasis on the effects of intrinsic structure and extrinsic specimen size. It was revealed that intrinsic interplanar interactions and rigidity of the network could be enhanced by a high temperature heat treatment, resulting in a transition from high plasticity to high elasticity. With the specimen size decreasing from a micrometer to nanometer scale, because of the reduction of weak links in the network, both the modulus and strength were dramatically enhanced along with a brittle-to-ductile transition. Molecular dynamics simulations unveiled the sliding, bending, buckling, collapsing, and densification mechanisms. Because of the size strengthening effects, a remarkable combination of compressive strength ≈1.7 GPa and yielding strain ≈15% was achieved for the nanoporous graphene nanopillars. The size effects revealed in this study bridge the gap between individual graphene sheets and carbon macromonoliths and are valuable for designing graphene-based materials and devices at multiple length scales.

Digest of
Tang D.-M., Ren C.-L., Zhang L., Tao Y., Zhang P., Lv W., Jia X.-L., Jiang X., Zhou G., Ohmura T., Huai P., Li F., Bando Y., Golberg D., Yang Q.-H.; Size Effects on the Mechanical Properties of Nanoporous Graphene Networks; Advanced Functional Materials, 2019, 29, 1900311; https://doi.org/10.1002/adfm.201900311.

Lithiation-Induced Dilation Mapping in a Lithium-Ion Battery Electrode by 3D X-Ray Microscopy and Digital Volume Correlation

Eastwood D. S., Yufit V., Gelb J. et al.

High-resolution 3D X-ray computed tomography (CT) enables detailed, non-destructive 3D structural mapping of a complete lithium-ion battery. By repeated 3D image acquisition (time lapse CT imaging) these investigations of material microstructure were extended into the fourth dimension (time) to study structural changes of the device in operando. By digital volume correlation (DVC) of successive 3D images the dimensional changes taking place during charge cycling were quantified at the electrode level and at the Mn_2O_4 particle scale. After battery discharging, the extent of lithiation of the manganese (III/IV) oxide grains in the electrode was found to be a function of the distance from the battery terminal with grains closest to the electrode/ current collector interface having the greatest expansion ≈30%) and grains furthest from the current collector and closest to the counter electrode showing negligible dilation. This implied that the discharge is limited by electrical conductivity. This new CT+DVC technique is widely applicable to the 3D exploration of the microstructural degradation processes for a range of energy materials including fuel cells, capacitors, catalysts, and ceramics.

Non-destructive microstructural investigation

Microstructural evolution, which can occur during processing and operation, is known to influence the performance and lifetime of energy materials including batteries, fuel cells, super capacitors, hydrogen storage media, and photocatalysts. While the impact of microstructural degradation can be severe, the mechanism of structural evolution at microscopic length scales is often poorly understood due to the difficulty of following such microstructural changes. Advances in non-destructive, high-resolution X-ray computed tomography (CT) offers new, quantitative insights into the behavior of these materials under operating conditions.

Tomographic imaging using X-rays and focused ion beams enabled researchers to obtain unprecedented insight into Li-ion batteries from the particle to the electrode and device level in three dimensions. Of these techniques, the uniquely non-invasive, high spatial resolution X-ray imaging method is particularly well suited to track changes in battery architecture and microstructure over time as the device ages and degrades. Earlier demonstrations have shown the versatility of synchrotron transmission X-ray microscopy to study in situ observations of 2D and 3D microstructural evolution for a range of materials. Coupled with digital volume correlation (DVC) this is a powerful technique that can quantify these dimensional changes over time and space.

3D X-ray microscopy

3D X-ray imaging was conducted on the full cell to elucidate the device architecture; this was achieved using a Xradia MicroXCT-400 laboratory X-ray microscope. A sequence of 1500 2000 × 2000 projections were obtained and reconstructed using a standard filtered back projection algorithm in the Xradia XMReconstructor software. A virtual cross-sectioned reconstruction of the cell is shown in Figure 1. From this device level scan, the cathode geometry was found to be cylindrical (diameter ca. 2300 µm height ca. 800 µm).

Although the device level scan provided the capacity to non-invasively determine the cell architecture without significant beam-hardening artifacts arising from the metal casing, the resolution and contrast for this imaging mode was not optimized to discriminate between the active and pore phases of the electrode. In order to achieve this, subsequent higher resolution region of interest (ROI) tomography was conducted using the Xradia Versa XRM-500 laboratory X-ray microscope. This system utilizes a novel geometry employing high detector resolution rather than relying on the traditional geometric magnification, enabling high resolution ROI scans for 3D structural quantification. A sequence of 2800 transmission radiographs were collected over 6 h both for the charged (generally less lithiated) and discharged (more lithiated) cathode states, using a voxel resolution of 1.25 µm and a 2000 × 2000 16-bit charge-coupled device (CCD) detector. The views were subsequently reconstructed using the Xradia XMReconstructor software.

Quantitative analysis

A comparison of the X-ray tomography of the cell in the charged and discharged states enabled the geometrical change associated with local state of charge to be linked to the electrochemical performance. Segmentation of the reconstructed data set demonstrated a reduction in porosity (the fractional space occupied by electrolyte and binder material between the $LiMn_2O_4$ grains of the electrode) upon charging, from 20.0 to 18.7 vol%, consistent with expectations regarding dilation of the manganese phase during

the $LiMn_2O_4$ to $Li_{1+x}Mn_2O_4$ phase change. While dissolution of the Mn phase is a known problem in manganese-based electrodes, the voltage required for this was not achieved and, as such, it was assumed that all measured volume changes are as a result of the $LiMn_2O_4/Li_{1+x}Mn_2O_4$ transition.

Particle tracking (PT) and DVC were used to explore the spatial variation in particle dilation as a function of battery state of charge. Figure 2 shows a tomogram of the full coin cell in the diametrical plane and the axial plane of the cylindrical electrode, respectively. The calculated displacement vectors (overlaid) showed a predominantly uniform 2–3% linear strain directed away from an anchor point of the cathode on the terminal positioned slightly off-center on the battery casing. The insets (Figure 2b–d) show magnified regions of the electrode, and in Figure 2e the authors show a 3D representation of the electrode dilation away from an anchor point.

Fig. 1: A cut-away image of the reconstructed cell, showing the manganese oxide cathode attached to the positive (uppermost) battery terminal.

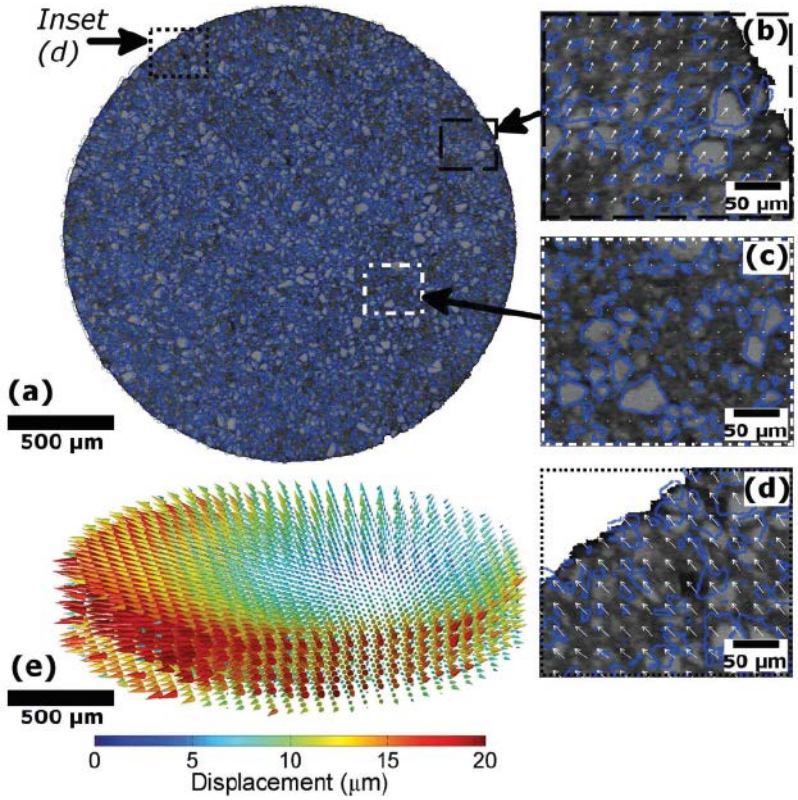

Fig. 2: a) Reconstructed radial slice (grayscale) through the central plane of the cylindrical cathode in the charged (delithiated) state, overlaid in blue with the positions of the Mn_2O_4 grains after battery discharge (lithiated). b–d) The displacement vectors of the grains as determined by DVC. The fixed anchor point in the cathode is in (d), with displacement extending outwards in all directions. e) A 3D representation of the displacement throughout the electrode in three-dimensional space (displacement magnitude is identified by cone color).

Summary

This work was the first to quantify the microstructural evolutionary processes in a functionally complete lithium ion battery in situ in three dimensions, providing a unique insight into the relationship between electrode microstructure and cell performance. The dilation of lithiated manganese oxide particles as a function of state of charge was found to be dependent upon the distance of individual grains in the electrode from the battery terminal, with grains furthest from the current collector showing least dilation. This implied that in this battery under examination lithiation was limited by electrode conductivity and not Li^+ transport through the electrode. This mechanism was observed for the ML414 electrode studied, which was considerably thicker than conventional electrodes; hence these potential drop effects may be more obvious than in different battery geometries with thinner electrodes. The extent of grain dilation was constant as a function of grain size, implying full lithiation to the core of individual grains, irrespective of grain size due to relatively fast lithium transport within grains.

3D X-ray microscopy is an extremely valuable tool for studies of this nature. Here these techniques have provided unique insight into the changing relationship between performance and microstructure in battery materials in situ and in operando. At a wider level the combination of X-ray CT and DVC/PT make it possible to track microstructural evolution and degradation across an array of important energy materials systems including: sintering in solid oxide fuel cells, coking and deactivation of catalysts, corrosion of PEM fuel cell microporous layers, thermal processing in hydrogen storage media, fracture and crack propagation in photovoltaics, degradation in gas diffusion layers, and mechanical processing of supercapacitor electrodes.

Digest of
Eastwood D. S., Yufit V., Gelb J., Gu A., Bradley R. S., Harris S. J., Brett D. J. L., Brandon N. P., Lee P. D., Withers P. J., Shearing P. R.; Lithiation-Induced Dilation Mapping in a Lithium-Ion Battery Electrode by 3D X-Ray Microscopy and Digital Volume Correlation; Advanced Energy Materials, 2013, 4, 1300506; https://doi.org/10.1002/aenm.201300506.

Multi-Scale Imaging of Polymer Electrolyte Fuel Cells using X-ray Micro- and Nano-Computed Tomography, Transmission Electron Microscopy and Helium-Ion Microscopy

Meyer Q., Hack J., Mansor N. et al.

Multi-length scale imaging of polymer electrolyte fuel cell (PEFC) membrane electrode assembly (MEA) materials is a powerful tool for studying, understanding and furthering improvements in materials engineering, performance and durability. A hot pressed MEA has been imaged using X-ray micro- and nano-computed tomography (CT), scanning electron microscopy (SEM), and recently developed helium-ion microscopy (HeIM). X-ray nano-CT was able to detect a volume containing all relevant fuel cell interfaces, from the carbon fiber of the gas diffusion layer (GDL) to the nafion membrane with a field of view of 65 µm and a pixel size of 64 nm. Features identified included linear marks on the carbon fiber surface, agglomerates of carbon nanoparticles in the microporous layer (MPL), and intrusion of the catalyst layer material into the Nafion membrane during the hot-pressing process. HeIM enabled imaging of a large area of MEA from tens of micrometers to sub-nanometers pixel resolution without any sample preparation, and captured similar features to X-ray micro-CT and nano-CT. Furthermore, at its highest resolution, the platinum and carbon catalyst nanoparticles could be distinguished at the surface of the catalyst layer, overcoming the limitations of SEM.

Complex hierarchical structure

PEFCs fuelled with hydrogen are among the most promising energy conversion technologies for a broad range of applications, including portable, stationary and automotive power delivery. As PEFCs have a complex hierarchical structure, with materials features ranging from nanometers to tens of micrometers, an array of multiscale imaging techniques is necessary to capture information at the required resolution/scale and to image the interactions and interfaces between materials.

The need to adopt different imaging techniques to access different length scales, positions within the membrane electrode assembly (MEA) structure and overcome challenges resulting from sample preparation constraints was evident. Due to the multi-scale aspects of the fuel cell structure, it was impossible to image a statistically relevant number of gas diffusion layer (GDL) fibers while also capturing resolved features of the catalyst layer (CL) and micro-porous layer (MPL) particles in the same field-of-view (FoV). As a result, imaging of these materials was typically done separately, using an array of techniques to achieve the target pixel size and sample size compromise, to image the feature of interest. In particular, helium ion microscopy (HeIM) was proving to be a powerful technique for the MEA study, which has not yet been applied to PEFCs.

Characterization techniques

X-ray micro- and nano-CT-3D imaging of MEA samples was performed with a Xradia 520 Versa or a Xradia 810 Ultra System from ZEISS. Reconstruction of the radiographs into a 3D volume for the micro-CT was achieved using a cone-beam filtered back-projection algorithm (Reconstructor Scout-and-Scan, ZEISS) resulting in a series of ortho-slices containing slice data in all three planes (xy, xz, yz) with isotropic voxel size of ~372 nm. Reconstruction of the radiographs into a 3D volume for the nano-CT was performed using a quasi-parallel filtered back-projection algorithm (Reconstructor Scout-and-Scan, ZEISS), resulting in an isotropic voxel size of ~63 nm). For all reconstructed volumes, X-ray post-processing and image segmentation were performed using Avizo Lite (Thermo Fisher) to segment the GDL layer material, consisting of large fibers bonded with PTFE, from the microporous medium, CL medium and the Nafion polymer membrane.

SEM sample analyses of the gas diffusion layer coated with MPL and 0.4 mgPt cm^{-2} CL (GDE) were carried out with a ZEISS EVO MA 10 with EDS (Inca X-act, Oxford Instruments). At high magnification, the use of a lateral secondary electron detector enabled the imaging of carbon nanoparticles of the CL with a pixel resolution of ~51 nm.

For HeIM imaging, circular GDE/MEA samples were examined with a Zeiss Orion Plus™ HeIM equipped with an Everhart-Thornley (ET) detector and collecting secondary electrons with a positive lattice bias of 500 V and an FoV of 12 mm to 700 nm.

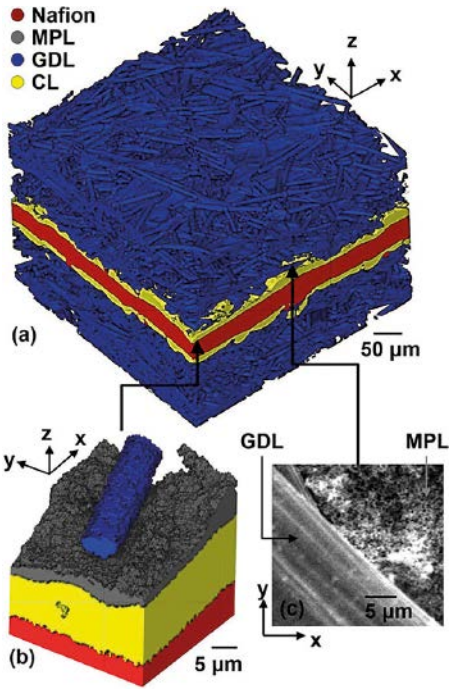

Fig. 1: Imaging of a hot-pressed fuel cell with pixel size from 372 nm to 51 nm. (a) Segmented CL, GDL and Nafion using X-ray µ-CT (FoV: 400 µm x 400 µm x 1,000 µm, pixel size: 372 nm); (b) segmented GDL, CL, MPL and Nafion using X-ray micro-CT (FoV: 32 µm x 32 µm x 42 µm, pixel size: 372 nm); (c) SEM image of the MPL and carbon fibers (FoV: 30 µm x 27 µm, pixel size: 51 nm).

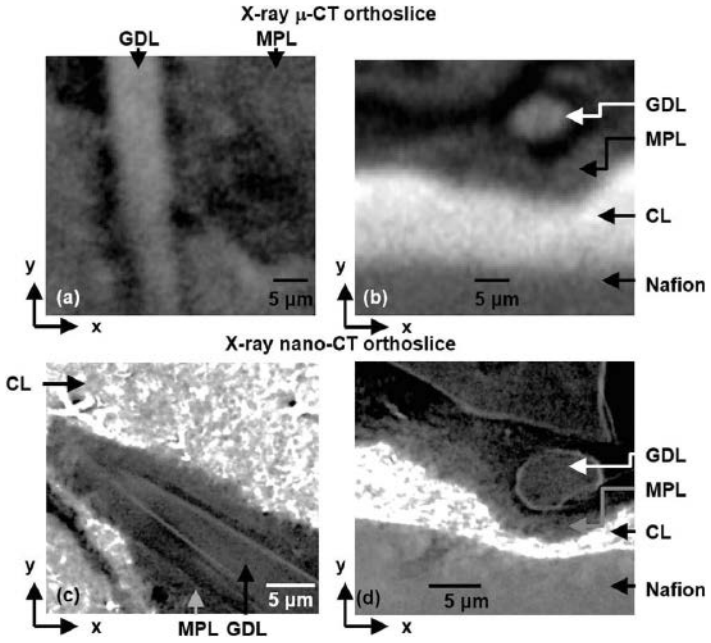

Fig. 2: (a–b) X-ray orthoslice of two similar samples of the hot-pressed fuel cell. Micro-CT (pixel size: 372 nm); (c–d) nano-CT (pixel size: 63 nm).

Spatial distribution of carbon fibers

Using X-ray micro-CT, the large FoV provided information regarding the spatial distribution of the carbon fibers of the GDL and information about macro-features of the CL and Nafion deformations could be obtained (Figure 1a). The area scanned was larger than the representative equivalent area of 0.1 mm^2; hence, the observations were representative and did not describe isolated features. Thus, it was possible to calculate the porosity across the fibers in multiple directions, the interfacial contact between the layers (CL/GDL, MPL/CL, Nafion/CL and Nafion/GDL), the CL crack size and the Nafion roughness factor.

However, this resolution was not sufficient to enable observation of features on the carbon fibers/MPL, which both appeared highly pixelated (Figure 1b). In addition, it was difficult to observe from this image the quality of the contact between the CL and the Nafion membrane. Although the SEM (Figure 1c) provided a better insight into the structure, with MPL nanoparticle agglomerate distinguishable, it is difficult to focus on these particles while imaging the fiber at the same time.

Therefore, an alternate approach has been used to image the same area, yet at a significantly higher resolution with X-ray nano-CT. The improvement in image resolution from X-ray micro-CT to X-ray nano-CT could be seen in the reconstructed orthoslices (Figure 2), with nearly six-times higher voxel resolution taken from similar locations on the samples imaged for micro-CT and nano-CT. Specifically, the fiber shape and its edges were far more visible, along with the Nafion/CL/MPL interfaces visible as a line (Figure 2c–d) instead of a blurry interfacial area (Figure 2b) challenging to reliably segment, and features of the MPL distinguishable from the background instead of observing it as a block.

Visualization of carbon and platinum (Pt) nanoparticles

Imaging of the carbon particles (CL/MPL) has been achieved using the HeIM. The carbon nanoparticles, across the same sample, appeared either densely packed, yet easily distinguishable (Figure 3b), or engulfed in a matrix-like structure, (Figure 3c). This structure could be solidified Nafion. However, the vast discrepancy between Figure 3b–c suggested that although an ionomer ink with a known Nafion content was added to the catalyst ink, local Nafion heterogenous concentrations existed within the solidified catalyst layer. Specifically, Nafion was concentrated in areas less dense in nanoparticles, which could form additional pathways for the proton and water transport across the catalyst layer, creating an effective 3-D electrode. To assess the ability of HeIM to image Pt nanoparticles coated on

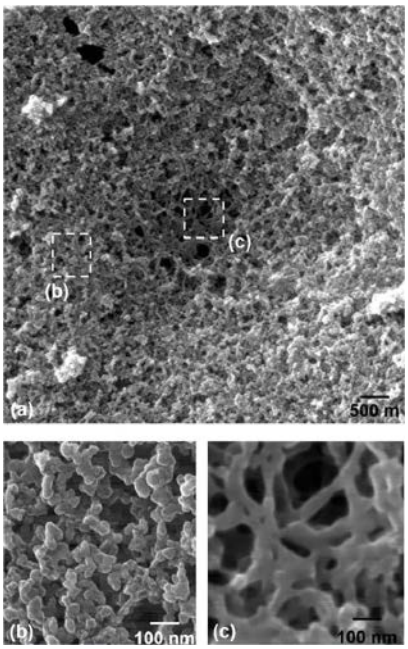

Fig. 3: Imaging of the CL coated on the MPL with pixel size from 10 nm to 1.2 nm with HeIM; (a) wide-scale structure of the CL (FoV: 7 µm x 7 µm, pixel size: 10 nm); (b–c) focus on nanofeatures (FoV: 660 nm x 660 nm, pixel size: 1.5 nm).

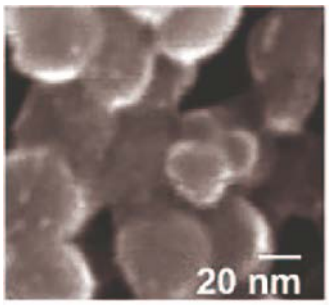

Fig. 4: Imaging of the Pt nanoparticles coated on carbon nanoparticles with the HeIM (FoV: 150 nm x 150 nm, pixel size: 0.5 nm).

carbon nanoparticles (Figure 4), the HeIM was used at its highest resolution. The HeIM revealed small bright particles coated onto the carbon nanoparticles of expected size range for Pt nanoparticles. In the process of imaging catalyst nanoparticles in technological MEAs, they were typically imaged before coating onto the MPL. The HeIM pixel resolution (~0.5 nm) could only provide a crude image of the Pt nanoparticles and was not sufficient to measure the particle size with accuracy. On the other hand, the HeIM enabled the imaging of the catalyst after coating onto the MPL. It was possible to distinguish the two materials, and the resolution enabled carbon particles with Pt catalyst to be distinguished from carbon particles of the MPL. Furthermore, the HeIM could enable observation of the CL particle density distribution after coating onto this MPL. This imaging method can be used to assess the effect of the catalyst ink preparation and deposition method onto the MPL to assess the quality of the CL/MPL interface.

Summary

Multi-scale characterization of MEAs provides the opportunity for gaining an in-depth insight into the interfaces and structural features of the MEA layer structure. The necessity of imaging samples taken from a fully assembled MEA was demonstrated, instead of probing and imaging subsystems, such as the CL coated onto the MPL, or MPL interactions with the GDL. This imaging study revealed new features, such as how the Nafion and CL are bonded together, how the CL is coated onto the MPL, how the carbon fibers influence the structure, and the patterning of the carbon fibers.

Different techniques revealed varying information, depending on the properties of interest. For the first time, the combination of X-ray nano-CT and HeIM microscopy has been applied to the study of PEFC MEAs, and enabled a relevant comparison across these techniques, highlighting their advantages and disadvantages. Over the other imaging techniques, the HeIM was superior as it has the combination of the following capabilities: (a) Imaging of insulating sample enabling it to image PTFE and Nafion with high resolution;

(b) imaging without coating at highest resolution with better contrast and improved depth of focus than SEM; (c) high surface sensitivity; (d) imaging of ultrathin layers, enabling imaging of the catalyst layer; (e) resist patterning; and (f) no image processing compared with computed tomography.

In addition, the HeIM microscope was able to detect features that can be identified with the other techniques and to overcome the resolution, the signal-to-noise ratio of X-ray micro-CT and nano-CT and the challenges of SEM depth-of-field. These were directly relevant to understanding the interactions between the different materials. The systematic cross-instrument methods used in this study for imaging are also directly relevant for other electrochemical materials such as Li-ion batteries, electrodes and solid electrolytes.

Digest of
Meyer Q., Hack J., Mansor N., Iacoviello F., Bailey J. J., Shearing P. R., Brett D. J.; Multi-Scale Imaging of Polymer Electrolyte Fuel Cells using X-ray Micro- and Nano-Computed Tomography, Transmission Electron Microscopy and Helium-Ion Microscopy; Fuel Cells, 2019, 19, 35-42; https://doi.org/10.1002/fuce.201800047.

Algorithmic Structural Segmentation of Defective Particle Systems: A lithium-Ion Battery Study

Westhoff D., Finegan D. P., Shearing P. R., Schmidt V.

In this article a segmentation algorithm that is able to identify defects (cracks, holes and breakages) in particle systems was described. This information was used to segment image data into individual particles, where each particle and its defects were identified accordingly. The authors applied the method to particle systems that appear in Li-ion battery electrodes. First, the algorithm was validated using simulated data from a stochastic 3D microstructure model, providing full information about defects. This allows users to quantify the accuracy of the segmentation result. Furthermore, it was shown that the algorithm can successfully be applied to tomographic image data from real battery anodes and cathodes, which are composed of particle systems with very different morpohological properties. Finally, the article revealed how the results of the segmentation algorithm can be used for structural analysis.

Defects in the microstructure of the materials under consideration occur under various conditions. A typical example of this phenomena are electrodes in lithium-ion batteries that undergo thermal runaway. In this process, which can be caused by extreme conditions such as high temperatures or overcharging, the temperature in the cell rises drastically, resulting in deformation of the particles in the electrodes. This deformation can be observed in tomographic images. Cracks, holes and breakages in the particles can strongly influence the underlying electrochemical and kinetic processes, as they lead to a higher surface area of the active material. For this reason, it is of high interest to analyze the occurrence of such defects by investigating which type of particles are susceptible to being damaged or which shapes the defects have.

In order to detect cracks, fractures and holes in particulate materials such as battery electrodes, the authors developed a new structural segmentation algorithm for tomographic image data.

Descriptions of the algorithm

For the conception of the algorithm the authors assumed that the tomographic image data are already preprocessed in a way that a binary image $\mathbf{I} : W \to \{0, 1\}$ exists, where $W \subset \mathbb{Z}^3$ is the observation window with $\mathbb{Z}$ being the set of integers. For each voxel $v = (x, y, z) \in W$ belonging to a particle, $\mathbf{I}(v) = 1$ is set, whereas for the remaining voxels $\mathbf{I}(v) = 0$ is defined. The remaining voxels include the pore space as well as further additives. This part is called the background phase in the following. The aim is to identify those background voxels where a defect of a particle is present. An example of the output of the algorithm is shown in Fig. 1, where particles are shown in different colors and defects are marked in blue. The basic idea of the single steps is described as follows. After closing holes using a cluster detection algorithm and marking them as defect voxels, further candidates for those defect voxels are identified based on the distance map. All candidates are initially added to the particle phase, and a further cluster detection is performed to identify possible new resulting holes. Given all candidates for defect voxels, the system of particle voxels and defect voxels is considered as one phase and segmented into individual particles using watershed techniques. Then, all candidates for defect voxels that belong to a watershed separator are removed. This, however, still leaves some wrongly chosen candidates for defect voxels, which are also deleted using a criterion that considers their local neighborhood. Finally, small clusters of defect voxels, which might result from small inaccuracies, are deleted. Due to the deletion of candidates, some particles together with their defects identified by the watershed algorithm might not be connected anymore, so the final set of particles is identified using a cluster detection algorithm, where small particles are considered as noise in the greyscale image and removed.

To show the broad applicability of the algorithm, Westhoff et al. used it for the segmentation of several data sets. For validation purposes, they generated simulated data describing the microstructure of a battery anode using the stochastic microstructure model described previously. By artificially inserting cracks, holes and breakages, the accuracy of the segmentation algorithm could be validated.

Application to tomographic image data

The practical application of the algorithm to tomographic image data for real electrode was demonstrated for a $LiCoO_2$ battery cathode and for a graphite anode each extracted from a commercial Li-ion cell. It must be noted that for these data sets no formal validation is possible, as the defects are unknown, however, the authors presented a comparison of greyscale images and corresponding segmentation to show that defects visible in the greyscale images are recognized in the segmentation. Subsequently, a statistical analysis of the segmented data sets was performed. Furthermore, it must be considered that the surface area calculated in this section was derived from the segmented tomographic reconstructions which is inherently limited by the resolution of the utilized X-ray computed

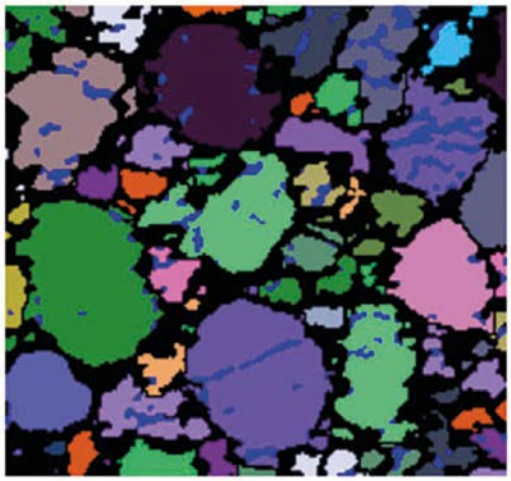

Fig. 1: *Final output of the segmentation algorithm, with particles labelled in different colors and defects shown in blue. Note that the algorithm is performed in 3D, but only the 2D slice is shown here.*

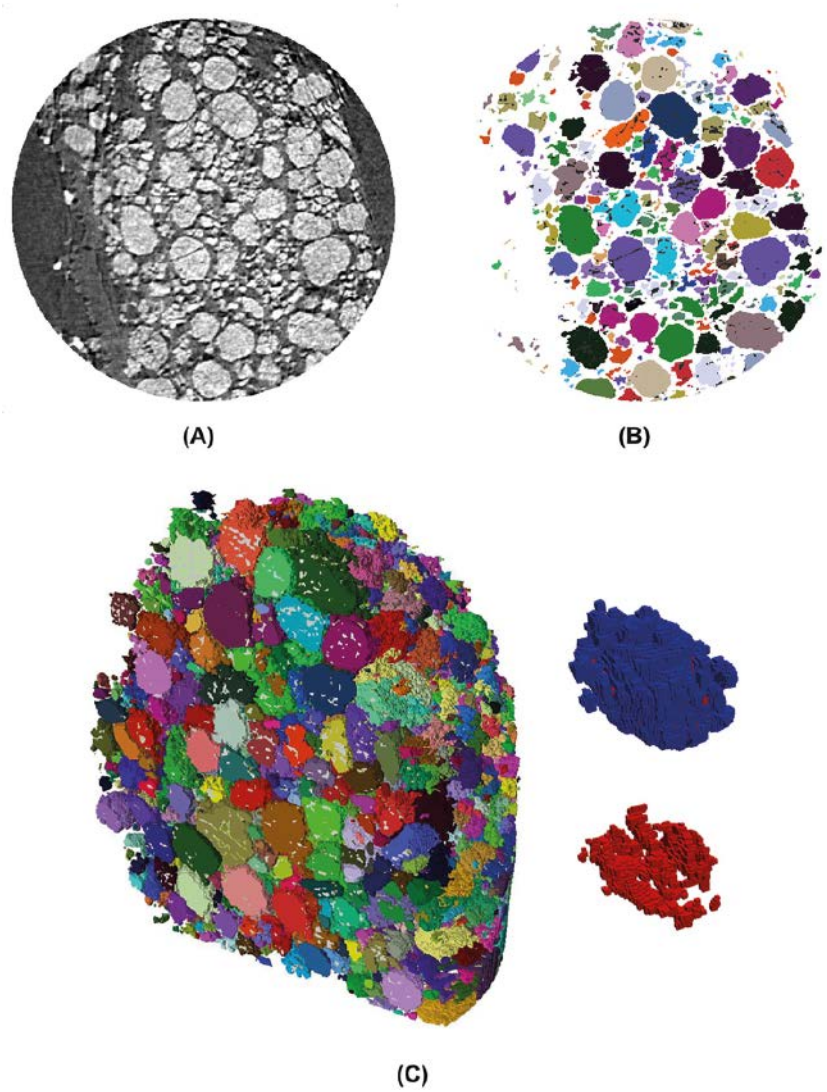

Fig. 2: *Results for $LiCoO_2$ data set. (A) Slice of the greyscale image. (B) Corresponding segmentation. Particles are shown in different colors and grey voxels indicate defects. (C) Left: 3D view of the segmented $LiCoO_2$ data set. Particles are shown in different colors, defects are marked in light grey. It should be considered that several slices at the front have been removed to allow a view 'inside' the structure. Right: Solid particle phase (blue) and its defects (red).*

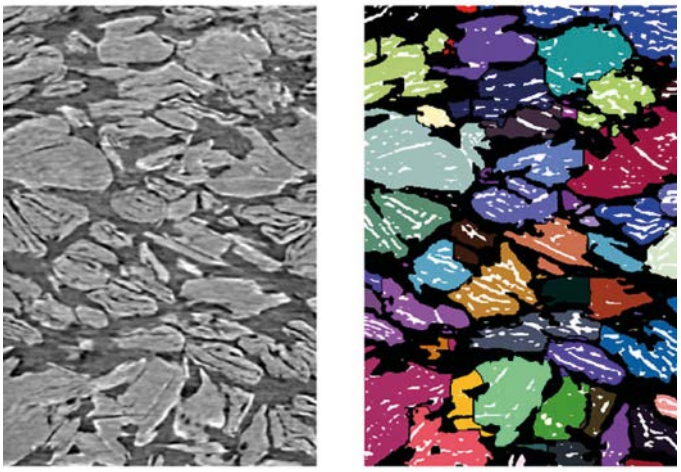

Fig. 3: Results for graphite data set. Particles are shown in different colors and white voxels indicate defects. Left: side view on a slice of the greyscale image. Right: segmentation corresponding to the left-sided picture.

tomography (CT) systems. For this reason, surface area comparisons provide a qualitative insight into the role of microstructural defects and, due to the limited surface texture details that can be captured, should not be interpreted to be actual specific surface areas of the material.

$LiCoO_2$

The particle size distribution of the $LiCoO_2$ electrode showed a significant reduction in the mean particle diameter following thermal runaway which is evidently caused by the decrepitation of particles (cracking and breakage) when exposed to the rapid increase in temperature (up to > 1000°C). The sample was imaged in a lab-based Zeiss Xradia Ultra 810 CT system with a pixel size of 63.1 nm. The radiographs were reconstructed using the Zeiss XMReconstructor software package, which uses an algorithm based on the standard filtered back projection.

Fig. 2 shows that a 2D slice of the 3D greyscale image (Fig. 2A) is compared to the corresponding 2D slice of the segmentation (Fig. 2B). The different colors indicate different particles, grey voxels indicate defects. Comparing the result to the greyscale image, it was found that defects visible in the greyscale slice are recognized in the segmented data set and the segmentation into individual particles mostly matches how one would label particles manually by visual inspection. In Fig. 2(C), a 3D view of the segmented structure is presented together with a view of an individual particle and its defects.

The analysis revealed that roughly 50% of the particles exhibit a defect. In electrodes, the active surface area of the particles is of high interest, because it significantly influences the ongoing processes. Therefore, we compute the surface area for the 3D image where all defects are added to the particles, i.e. no defects are present, and for the defective particle system, where we only close holes, as they are not reachable from the pore space. It could be observed that the defects increase the specific surface area by more than 20%, which would significantly affect the rate capability of the lithium ion cells as well as the reaction rate of the $LiCoO_2$ during thermal runaway.

Graphite

For this analysis, a section midway between the surface of the electrode and the current collector was imaged and analyzed. The graphite electrode was imaged using both Zernike phase and absorption contrast imaging modes in a lab-based CT system (Zeiss Xradia Ultra 810, Carl Zeiss XRM) with a pixel size of 126.2 nm. The phase and absorption contrast images were reconstructed using a Zeiss XMReconstructor and were thereafter blended.

The graphite particles are not spherical, but have rather the form of flakes as shown in a side view (Fig. 3C and D).

Image analysis revealed that the percentage of defective particles is about 18% here, which at first view looks different from the visual impression. However, there are many very small particles which do not exhibit cracks, and rather the larger graphite flakes predominantly have cracks. The influence of cracks on the active surface area of the graphite is much greater than in the case of the $LiCoO_2$ due to its flake-like microstructure, contributing to more than a 70% increase in surface area when compared to the equivalent microstructure without cracks.

Summary

A structural segmentation algorithm for image data was introduced that detects cracks, breakages and holes in particulate systems and performs a segmentation into individual particles, where fragments of one and the same particle are recognized accordingly. The algorithm has been validated using simulated data from a stochastic 3D microstructure model, where positions of defects are known. This allows a quantification of the accuracy of the algorithm. Finally, the method has been applied to tomographic image data from a battery anode and cathode, which exhibits its broad applicability for data sets with different defects with a reasonable range of sizes. If very fine and much bigger defects occur in one and the same structure, the algorithm might have problems and it could be helpful to consider both scales individually. Moreover, the structural segmentation algorithm allows for a comprehensive analysis of defects in particle systems. In particular, the spatial frequency of defects is of high interest.

Digest of
Westhoff D., Finegan D. P., Shearing P. R., Schmidt V.; Algorithmic structural segmentation of defective particle systems: a lithium-ion battery study; Journal of Microscopy, 2017, 270, 71-82; https://doi.org/10.1111/jmi.12653.

The Effect of Ink Dilution and Evaporation on the Microstructures of Catalyst Layers in Polymer Electrolyte Membrane Fuel Cells

Zhao J., Li X., Liu Z.

The microstructures of catalyst layers (CLs) in proton exchange membrane fuel cells determine cell performance and durability. Delicate ink preparation processes and coating/drying processes affect the resulting microstructures including active sites, pore networks, ionomer networks and Pt/C networks. This article reported experimental observations of the effect of ink dilution and evaporation condition on the microstructures. The microstructures of dried ink droplets were presented and compared among different dilution ratios and different evaporation conditions in terms of the spatial distributions of carbon supported platinum (Pt/C) particles, ionomers, and pores. It was observed that ink dilution ratio and evaporation condition can significantly alter resulting microstructure patterns through affecting viscosity and particle flow patterns during the evaporation. More concentrated solution made catalyst inks less spread out on a substrate surface, leading to larger droplet height and larger contact angle. Ambient relative humidity had a significant impact on catalyst deposition patterns. Under low relative humidity condition, catalyst particles were concentrated both near the central and the periphery of the droplet; while under high relative humidity, the central part was uniform, and the particles moved towards the edge of the deposition, forming a stripe-like structure. This indicated that ink dilution and evaporation is key to the CL microstructure formation.

PEM fuel cells

A polymer electrolyte membrane (PEM) fuel cell is a device that converts the chemical energy stored in fuels and oxidants directly into electric energy through electrochemical reactions. The electrochemical reactions occur in an ultra-thin porous region (typically 5-40 μm thick), which is known as the catalyst layers (CLs) in PEM fuel cells. The CL is conventionally composed of catalyst particles, ionomers, and pores for providing the functional microstructures that have sufficient number of active sites for reactions, pathways for proton and electron transport, and channels for reactant gas delivery and water management.

Microstructure analysis of CLs

Earlier studies indicate that the inhomogeneity of the microstructures of the CLs at different length-scales is not only essential for the required functions but also a root reason for degradation and malfunction in PEM fuel cells. The CL microstructures can be affected by many factors, including catalyst ink composition, ink preparation, and ink application. Furthermore, the solvent evaporation process determines initial CL microstructures when ink composition, ink preparation procedure, and ink application method are fixed. The solvent evaporation is mainly influenced by two major factors: solvent composition and evaporation condition.

Since it has not yet been well understood, the effect of solvent evaporation on the CL microstructure formation was investigated in the present study. For this purpose, catalyst ink droplets were placed on a microscope slide, and the drying process is observed under an optical microscope (Carl Zeiss, Axio Zoom V16). The drying dynamics and the resulting microstructure were tested with various solvent compositions and evaporating conditions. In addition, the intensity analysis of the microscope images was conducted for the catalyst deposition to quantify the material distribution and thickness variations.

Microstructure formation processes

After catalyst inks (CLs) were coated on a substrate, the solvent in the inks began to evaporate and as a result the microstructures of CLs were formed. To evaluate the microstructure formation processes - in particular the formation of Pt/C networks, ionomer networks, and pore networks - this study showed the microstructures of dried ink droplets that had different dilution ratios (1:50, 1:100, 1:200, and 1:400) and were dried under different evaporation conditions (relative humidity of 0.56 and 0.28 with the same room temperature of 296.1 K and pressure of 99.4 kPa).

The shape of the droplets was regarded as a spherical cap. On the basis of the spherical-cap-shape assumption, with the measured contact line diameter of the 1 μL ink droplet, the corresponding contact angle and droplet height could be determined mathematically. For a consistent comparison, the equilibrium contact angle was defined as the contact angle when the droplet first reached its maximum diameter, while the receding contact angle was defined as the contact angle when the contact line began to recede. Figure 1 demonstrates the determination of the contact angle and height of a sessile spherical-cap droplet on a flat surface.

Effect of solvent dilution ratio

It could be shown that a more concentrated solution (e.g. with a dilution ratio of 1:50)

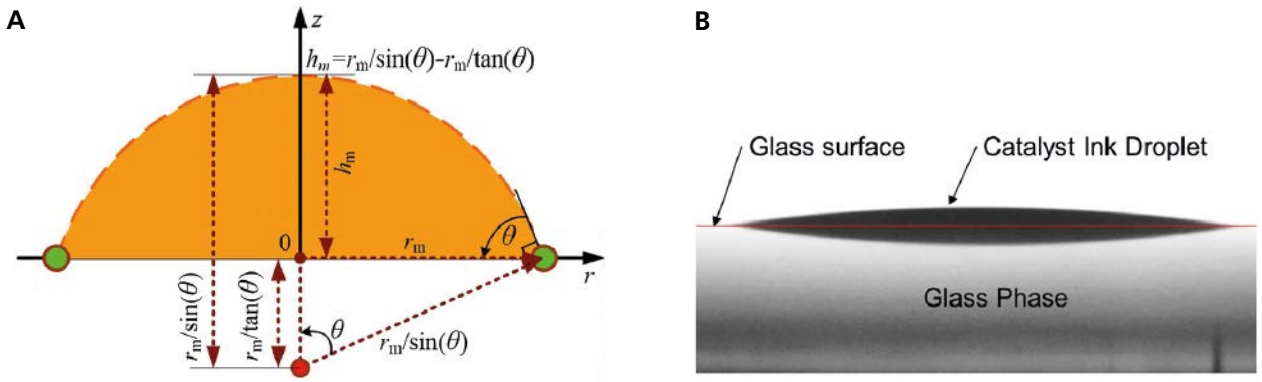

Fig. 1: Schematic of the determination of the contact angle and height of a sessile spherical-cap droplet on a flat surface: (A) geometric dimension and (B) a typical ink droplet from side view.

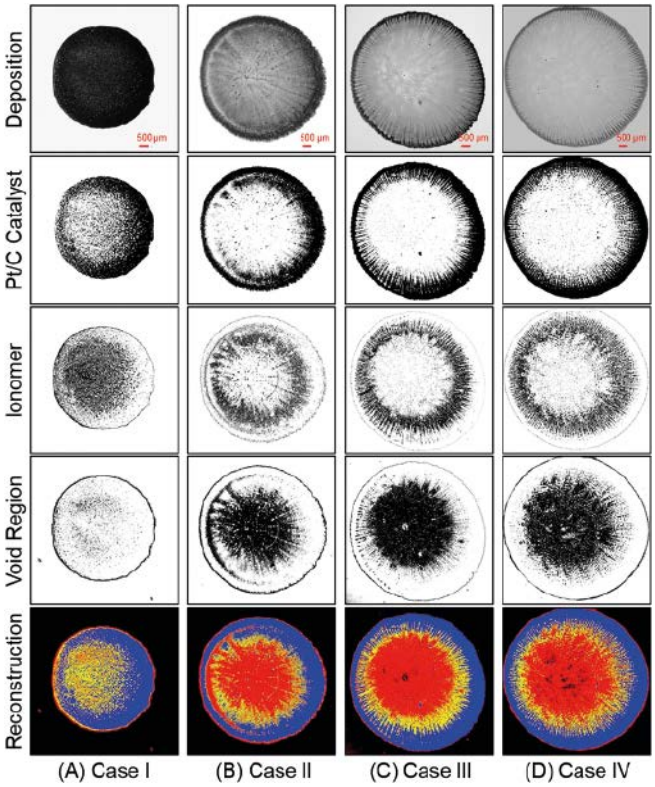

Fig. 2: Phase separation and microstructure reconstruction of the catalyst ink deposition with various dilution ratios of 1:50 (Case I), 1:100 (Case II), 1:200 (Case III) and 1:400 (Case IV) (For the fifth row, the blue, yellow, red, and black colours represent the Pt/C, ionomer, and pores).

distributes the catalyst ink less on the surface of the substrate with a larger drop height (up to 70.3 µm) and a larger contact angle of the catalyst drop (up to 2.68°). In contrast, the droplet was distributed more strongly on the substrate surface as the solvent content increased. Increasing the droplet diameter automatically means a higher exposure to the ambient air, which leads to a faster evaporation rate of the solvent.

To monitor the effect of dilution ratios on the material (solid) distribution in the deposition, the phase separation and reconstruction were conducted based on the assumption that each phase in the deposition (e.g., catalysts, ionomers, and pores) is represented by a range of grey values in the microscopy images, and the area fraction of each phase can be estimated by its volumetric fraction in space.

The phase separation and reconstruction of the four dilutions types (Case I–IV) of ink droplet deposition processed using numerical calculations are presented in Figure 2. It could be determined that a large portion of the catalyst particles are accumulated at the edge of the deposition when the ink was diluted by the solvent (e.g., Case II, III, and IV), and very few catalyst particles are present at the central part. The majority of

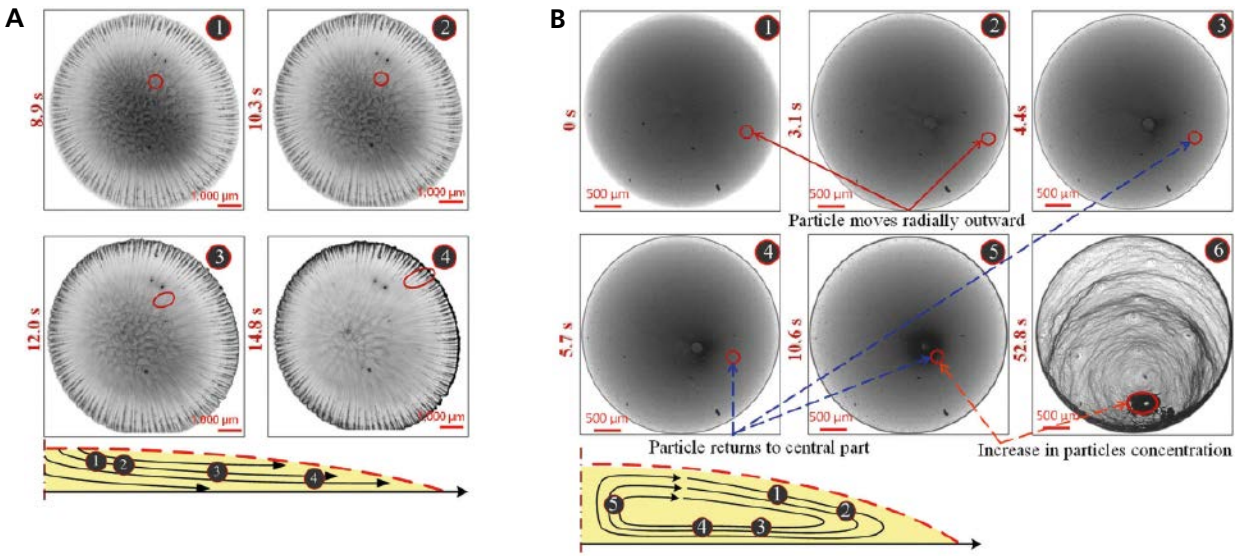

Fig. 3: Particle transport in the ink droplets under (A) condition 1: relative humidity of 0.56 and (B) condition 2: relative humidity of 0.28 (The markings 1-4 and 1-6 in the top view figures means the sequence of the figures as the evaporation proceeds, or at different evaporation time shown on the right of each image, and those in the side-view figures demonstrate the locations of traced particles in the droplets).

Nafion polymer was located closer to the central part than the particles, and pores dominated at the central part, indicating the central part was not well covered by catalyst deposition. Additionally, it was evident that catalysts and ionomer were not uniformly distributed in the depositions. While for the concentrated ink (e.g., Case I), material distribution was relatively uniform in comparison with the other three cases. The image analysis indicated that dilution ratio had a strong impact on the microstructure formation of the catalyst deposition. Additionally, it was observed that as the dilution ratio was increased, the surface of the catalyst ink deposition became rougher.

Effect of evaporation condition

The experimental results also indicated that the evaporation condition, especially the relative humidity, also significantly affected the microstructure of the CLs. Under a high relative humidity (e.g., 0.56), the droplet was more spread out on a flat surface with a larger contact diameter and a lower height, and the particles moved radially outward and accumulated at the edge of the depositions as shown in Figure 3A, with some stripe patterns left near the edge.

On the other hand, for a lower relative humidity (e.g., 0.28), the contact diameter was much smaller and the initial droplet height was much larger. A strong circulation flow inside the droplet was generated. The catalyst particles first migrated radially to the edge of the droplets, with some of the particles deposited near the contact line (coffee ring effect), and some others migrated radially back to the central part, leading to a more concentrated solution at the central part, as shown in Figure 3B.

Summary

In this work, catalyst inks (CLs) were applied to substrates in various dilutions, and the solvent was then evaporated under various conditions so that the microstructures could be analyzed by optical microscopy. The catalyst inks were prepared in dilution ratios of 1:50, 1:100, 1:200 and 1:400, and the experiments were performed under different room conditions with a focus on relative humidity of 0.56 and 0.28 at the same room temperature of 296.1 K and a pressure of 99.4 kPa. It was found that a more concentrated solution distributed the catalyst ink less on the surface of the substrate with a larger drop height and a larger contact angle of the drop. As the solvent content increased, the droplets were distributed more strongly on the substrate surface and at the same time the catalyst particles were distributed more unevenly with a significantly higher surface roughness. In addition, the results indicated that evaporation conditions, especially relative humidity, also significantly affect the microstructure of the CLs. A lower relative humidity (e.g. 0.28) impeded particle transport and caused a coffee ring phenomenon at the edge of the deposits and a distinct bump (or particle concentration) at the central part. This study indicated that the dilution ratio of the catalyst inks and the evaporation conditions have a significant influence on the CL microstructure and therefore need to be controlled to achieve the quality and consistency required for practical CL production.

Digest of
Zhao J., Li X., Liu Z.; The effect of ink dilution and evaporation on the microstructures of catalyst layers in polymer electrolyte membrane fuel cells; International Journal of Energy Research, 2019, 43, 6799-6811; https://doi.org/10.1002/er.4671.

Imaging Electrochemical Processes: An Interview with Paul Shearing

Paul Shearing is Professor of Sustainable Energy Engineering at the Department of Engineering Science and Director of the ZERO Institute at Oxford University. He holds the Royal Academy of Engineering Chair in Emerging Battery Technologies. He was elected a Fellow of the Royal Academy of Engineering in 2024. He is an expert in the study and design of electrochemical processes in devices such as fuel cells, batteries and electrochemical reactors.


© UCL Department of Chemical Engineering

As the mobile world puts its trust in the Li-ion battery, it is the most important energy storage technology of today. Especially for small electronics, electrochemical energy storage with lithium-ion batteries is the method of choice due to their ability to deliver high energy and power densities. Lithium-ion batteries are also the key technology for electric vehicles and will contribute significantly to the balance of supply and demand of regenerative energies.

Electrochemical technologies will play a role across a range of energy storage and conversion applications, for example solid oxide fuel cells (SOFC) – one of the high-temperature variants of fuel cells – offer the highest electrical efficiencies of up to 60 percent. They can be used for domestic energy supply, industrial combined heat and power generation, power generation in power plants and on-board power generation in vehicles. They can be operated with hydrogen, but also with methane (i.e. natural gas) or other reformed fuels.

Together with his colleagues and partners, Paul Shearing frequently uses correlative X-ray microscopy analysis to observe the electrochemical processes and changes in energy materials.

1. Paul, if you compare the individual electrochemical technologies that you and your team are investigating, which of these technologies do you believe have the greatest development potential?

We research a range of electrochemical energy conversion and storage devices; including Li-ion batteries which are widely applied today, to next generation batteries such as Li-Sulfur and Na-ion; alongside fuel cells, redox flow batteries and super-capacitors. Across this portfolio of electrochemical technologies there is huge potential to 'mix-

and-match' the right technology to the right application, balancing various requirements for energy and power density, cost, volume, weight and safety. Of these technologies, the Li-ion battery has had the greatest impact on society to date, but moving forward, it is impossible to highlight a single technology as having the greatest *potential* – I believe that a portfolio of electrochemical technologies will emerge working together to service a range of needs.

2. What are the benefits of your research with regard to the energy supply of the future? What visions do you have for this?

We use a range of characterisation and diagnostic tools to understand how the materials inside electrochemical technologies operate, age, degrade and fail. This gives us insight into how we can better design materials for next generation devices. Over the past ten years we have developed tools for in-situ and operando investigations, so we can see the materials operating in their native environments; as well as tools for characterisation across multiple length scales – for example understanding a Li-ion battery from a single nano-particle up to a full device. Our vision is to apply these tools to accelerate the commercialisation of electrochemical technologies, reducing the time it takes to discover materials in the lab to deploying them in prototype devices, and ultimately making commercial products that have a positive influence on society.

3. In your opinion, to what extent can electrochemical technologies permanently guarantee the growing demand for energy supply in the future? What potential and what difficulties do you see in this?

The work that we focus on is predominantly associated with electrochemical energy conversion and storage – so these are not devices that directly generate energy – rather they store energy (for example in a battery) or convert energy (for example the conversion of hydrogen and oxygen to water, electricity and heat in a fuel cell).

These technologies do have a significant role to play in the emerging energy landscape, not only as power sources for electric vehicles, but also to balance the energy supply from renewable sources, such as wind and solar, which are inherently intermittent. For example, large batteries can be installed alongside solar arrays to store electrical energy, or electrolysers to make hydrogen can be installed alongside wind-farms; this helps to offset the energy usage to a time when it can be useful, and maximises the benefit of these renewable resources.

4. Which of the technologies you are studying is viewed more critically in society and which more uncritically?

In general, we find that people are hugely excited by electrochemical technologies – people understand the need for climate action, and therefore have an enthusiasm for the technologies that will help us reduce carbon emissions, improve air quality and grow sustainably.

When it comes to electric vehicles, we have seen huge progress in the past decade, and people are excited about electric vehicle ownership. Nonetheless, people expect electric vehicles to largely be a drop-in replace-

© UCL Department of Chemical Engineering

ment for their combustion engine cars – so that means there are concerns about range anxiety and charging times for battery powered vehicles, and the availability of hydrogen re-fuelling infrastructure for fuel cells cars. These are areas that are being actively researched to try and address public concerns.

5. What have been the milestones in the development of imaging technology since your research in electrochemical technologies?


© UCL Department of Chemical Engineering

When we first started using X-ray tomography for imaging electrochemical devices, most of our work was at synchrotrons, large particle accelerators that are operated as international research facilities – the availability of 'beam time' would often restrict the number of experiments we could do, so the translation of synchrotron capability to the lab environment has been hugely enabling for us.

We continue to also work extensively with synchrotron radiation, and are amazed by the pipeline of developments in techniques available there – ten years ago we would collect 1TB of data per day; now we can collect that in around a minute, which provides an indication of how the techniques have grown, particularly in their ability to capture time resolved data, very quickly.

6. You work extensively with correlative X-ray microscopy. What advantages does this method offer you in your work and which areas of application have not yet exhausted the potential of this technology in your opinion?

One of the major advantages of X-ray imaging is that it is inherently non-destructive, so we can explore the evolution of materials over time in response to a range of conditions. This has been pivotal for us to understand how materials operate in devices, and how they change over time. We still have lots of avenues to explore – there is a constant stream of new materials innovations, so we now have a toolbox to provide new insight into their operation, which can help to evaluate and optimise materials more rapidly.

7. What has been your most important insight into battery or fuel cell technology to date, where modern imaging methods have served you well?

There are many examples – ranging from super high-speed imaging to understand how batteries fail, imaging fuel cells under-operating conditions to see how catalyst layers evolve, performing nano-CT at high temperatures to evaluate processing parameters for ceramic fuel cells, and mimicking battery materials processing via in-situ compressions… we use correlative imaging across a range of length scales and applications, which, in tandem with simulation tools, continues to deliver exciting new insight.

8. What expectations do you have of equipment and software development with regard to the further improvement of microscopic analyses in your research area?

We are always keen to do things faster, at higher spatial resolution, and on larger samples – so anything that helps us to achieve this is a critical development for us.

Thank you very much for this interview, Paul.

Interview with Prof. Paul R. Shearing from the Department of Chemical Engineering, University College London, UK

Deepen your knowledge.

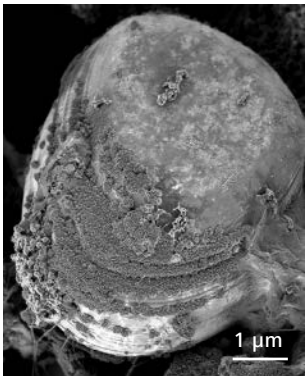

ZEISS Crossbeam 550

No matter whether you are milling, imaging or performing 3D analytics. Enjoy working with ZEISS Crossbeam – your FIB-SEM for high throughput 3D analysis and sample preparation. Exploit insights in your samples in 2D and 3D. Process any sample on a nanoscopic scale: The Ion-sculptor FIB minimizes sample damage while maximizing sample quality.

zeiss.com/crossbeam

ZEISS

Seeing beyond